VLF Measurements of the Poynting Flux
Along the Geomagnetic Field With the
Injun 5 Satellite[*]

by

Stephen R. Mosier[**]

A thesis submitted in partial fulfillment of the
requirements for the degree of Doctor of Philosophy
in the Department of Physics and Astronomy
in the Graduate College of
The University of Iowa

January 1970

Thesis supervisor: Associate Professor Donald A. Gurnett

Graduate College
The University of Iowa
Iowa City, Iowa

CERTIFICATE OF APPROVAL

————————————

PH.D. THESIS

————————————

This is to certify that the Ph.D. thesis of

Stephen R. Mosier

with a major in Physics has been approved
by the Examining Committee as satisfactory
for the thesis requirement for the Ph.D.
degree at the convocation of January 1970.

Thesis committee: _____
Thesis supervisor

_____
Member

_____
Member

_____
Member

_____
Member

ACKNOWLEDGEMENTS

ABSTRACT

The direction of the Poynting flux, up or down the geomagnetic field, has been determined for several types of very-low-frequency (30 Hz to 10 kHz) radio noise phenomena observed with the Injun 5 satellite, thereby providing information about the source region of these waves and their propagation in the magnetosphere. Determinations of the Poynting flux direction of short-fractional-hop whistlers and proton whistlers show that they are propagating up the geomagnetic field in accordance with the accepted theories of these phenomena, thereby providing a good check on the experimental technique. Measurements are presented on the Poynting flux direction of subprotonospheric whistlers, periodic emissions, ELF hiss, chorus, VLF hiss, and a new type of emission called a saucer. A new propagation phenomenon has been found in which ELF hiss may propagate across the plasmapause boundary to lower latitudes and become subsequently reflected and trapped within the plasmasphere. A new type of sub-auroral-zone VLF hiss has been found, and it is shown that the observations of VLF hiss are consistent with emission mechanisms proposed by other investigators in which hiss is generated by Cerenkov radiation. The saucer-shaped emissions are found to be propagating

upward from a source below the satellite. A qualitative explana-

tion of the frequency-time shape of this new type of emission is

presented.

TABLE OF CONTENTS

TABLE OF CONTENTS (Continued)

LIST OF FIGURES

LIST OF FIGURES (continued)

LIST OF FIGURES (continued)

Page

FOREWORD

This thesis presents the results of the first direct measurements of the direction of propagation, along the geomagnetic field, of very-low-frequency electromagnetic waves in the earth's magnetosphere. The initial results of these measurements were reported in a paper delivered to the 1969 spring meeting of the International Scientific Radio Union entitled "VLF Measurements of the Component of the Poynting Flux Along the Geomagnetic Field with the Injun 5 Satellite," by Stephen R. Mosier and were subsequently published in two papers in the Journal of Geophysical Research, entitled "Initial Observations of VLF Electric and Magnetic Fields with the Injun 5 Satellite," by Donald A. Gurnett, G. William Pfeiffer, Roger R. Anderson, Stephen R. Mosier, and David P. Cauffman [Gurnett et al., 1969] and "VLF Measurements of the Poynting Flux Along the Geomagnetic Field with the Injun 5 Satellite," by Stephen R. Mosier and Donald A. Gurnett [Mosier and Gurnett, 1969].

In addition to the results described in the three papers above, this thesis presents a detailed error analysis of the Poynting flux measurement as well as detailed studies of ELF hiss and VLF hiss by the Poynting flux measurement technique which have not been previously reported.

I. INTRODUCTION

There exists a considerable body of data on magnetospheric very-low-frequency (VLF) radio noises [Helliwell, 1965]. Although the characteristics and "in situ" distributions of VLF waves in the magnetosphere can often give some indication of the source regions of these noises [see, for example, Russell et al., 1969; Burtis and Helliwell, 1969], no measurements have been made to directly determine the source locations. Since the emission mechanisms are usually very dependent upon the plasma parameters in the source region, it is of fundamental importance to establish the source regions of these noises, particularly whether the noises are generated at low altitudes near the base of the ionosphere or at much higher altitudes in the magnetosphere. In addition, since the spectral forms of many VLF emissions are determined by the waves' propagation through the ionosphere and the magnetosphere, it is of primary interest to be able to determine the direction of propagation of the observed waves. This thesis presents the results of measurements of the Poynting flux direction, up or down the geomagnetic field, of VLF electromagnetic waves in the frequency range from 30 Hz to 10 kHz using the NASA/University of Iowa Injun 5 satellite.

The Injun 5 satellite was launched on 8 August 1968 into an elliptical orbit with an inclination of 80.66°, an apogee altitude of 2528 km, and a perigee altitude of 677 km. The experiments on board Injun 5 include a VLF electric and magnetic fields experiment, a dc electric field experiment, a set of low-energy proton and electron differential energy analyzers, an array of solid-state high-energy electron and proton detectors, and an electron density and temperature probe. A detailed description of the VLF experiment has been given by Gurnett et al. [1969] and only those aspects of the experiment pertaining to the Poynting flux determination will be presented here. The VLF experiment consists of one electric dipole antenna, one magnetic loop antenna, two wide-band (30 Hz to 10 kHz) receivers, a narrow-band step-frequency receiver, and an impedance measurement for determining the electric antenna impedance.

The spacecraft is magnetically oriented by a bar magnet within the spacecraft such that, when properly aligned, the x-axis of the spacecraft is parallel to the geomagnetic field with the positive x-axis downward in the northern hemisphere. Typical maximum alignment errors between the x-axis and the geomagnetic field after about mid-December 1968, when magnetic alignment was achieved, are about ten degrees. When magnetically oriented,

the electric antenna axis (y-axis) and the magnetic antenna axis
(z-axis) are perpendicular to the geomagnetic field as well as
to each other. This antenna geometry is illustrated in Fig. 1
and, as discussed in the next chapter, has the feature that the
direction of the Poynting flux, up or down the geomagnetic field,
can be determined from the time-averaged product of the electric
and magnetic antenna signals.

The electric and magnetic wide-band receivers each consist
of two band-pass filters providing a low-frequency band of 30 Hz
to 650 Hz and a high-frequency band of 300 Hz to 10 kHz, which
are independent of each other. These frequency bands are called
the "low" and "high" bands, respectively. Following the band-
pass filters, a compressor amplifier compresses the dynamic range
of the broadband ac signals from the antenna (80 dB) to a dynamic
range (20 dB) suitable for direct telemetry to the ground. The
electric and magnetic telemetry signals are synchronously
demodulated at the ground station, thus preserving the relative
phase between the electric and magnetic receiver outputs. The
electric receiver output is interrupted for 8 seconds in every
30 seconds for telemetry of the electric antenna impedance
measurement.

II. THE THEORY AND TECHNIQUE OF THE INJUN 5
POYNTING FLUX MEASUREMENT

A. The Theory of the Measurement

A magnetically oriented satellite provides an ideal platform
for the measurement of the Poynting flux direction. For a single
plane wave propagating in a cold plasma at a frequency less than
the electron plasma frequency, Maxwell's equations and the cold
plasma equations of motion relate the components of the electro-
magnetic field in such a way that the sign of the Poynting flux
$\vec{S}$ can be determined from the measurement of a single electric
field component and an orthogonal magnetic field component. Thus,
the direction of $\vec{S}$, up or down the geomagnetic field, can be
determined under very general conditions using just one electric
and one magnetic antenna.

To prove this result consider a wave propagating in the
x-z plane at an angle θ to the static magnetic field. Let the
z-axis be parallel to the static magnetic field. Using the
eigenvalue equation for the electric field vector,

$$\begin{pmatrix} S - n^2 \cos^2 \theta & -iD & n^2 \cos \theta \sin \theta \\ iD & S - n^2 & 0 \\ n^2 \cos \theta \sin \theta & 0 & P - n^2 \sin^2 \theta \end{pmatrix} \begin{pmatrix} E_x \\ E_y \\ E_z \end{pmatrix} = 0 \ ,$$

where S, P, and D are the dielectric tensor elements defined by Stix [1962], and Maxwell's equation

$$\vec{n} \times \vec{E} = c\vec{B} \ ,$$

the fields in the x-y plane are

$$E_x = e_x \cos(-\omega t) \ , \qquad B_x = b_x \sin(-\omega t)$$
$$E_y = e_y \sin(-\omega t) \ , \qquad B_y = b_y \cos(-\omega t)$$
$$E_z = e_z \cos(-\omega t) \ , \qquad B_z = b_z \sin(-\omega t)$$

where

$$e_x = E_o \ , \qquad\qquad b_x = \frac{-n \cos\theta}{c} \left(\frac{D}{S - n^2} \right) E_o$$

$$e_y = \left(\frac{D}{S - n^2} \right) E_o \ , \qquad b_y = \frac{n \cos\theta}{c} \left(\frac{P}{P - n^2 \sin^2\theta} \right) E_o$$

$$e_z = -\left(\frac{n^2 \cos\theta \sin\theta}{P - n^2 \sin^2\theta} \right) E_o \ , \qquad b_z = \frac{n \sin\theta}{c} \left(\frac{D}{S - n^2} \right) E_o$$

Since the wave normal direction is, in general, unknown the satellite coordinates (primed) will be rotated from the above unprimed coordinates by an arbitrary and unknown angle ψ around

the static magnetic field (z-axis), relative to the wave vector in the x-y plane. In addition, if the satellite is not perfectly oriented, the x and y axes will be further displaced by angles labeled δ_E for the x-axis and δ_B for the y-axis. This geometry is illustrated in Fig. 2. If we assume that δ_E and δ_B are sufficiently small so as to both be orthogonal to ψ, then the transformed fields in the satellite frame of x'-y' reference are

$$E_{x'} = (E_x \cos \psi + E_y \sin \psi) \cos \delta_E + E_z \sin \delta_E$$

$$B_{y'} = (B_y \cos \psi - B_x \sin \psi) \cos \delta_B + B_z \sin \delta_B \ .$$

The Poynting flux along the z-axis is

$$S_z = E_x H_y - E_y H_x = \frac{1}{\mu_o}(E_x B_y - E_y B_x) \ . \tag{1}$$

Computing time averages, denoted by the symbol $\langle \ \rangle$, over one complete period of $\cos(-\omega t)$, the average Poynting flux along the z-axis is

$$\langle S_z \rangle = \tfrac{1}{2} E_o^2 \frac{n \cos \theta}{\mu_o c} \left[\frac{P}{P - n^2 \sin^2 \theta} + \left(\frac{D}{S - n^2} \right)^2 \right] \ . \tag{2}$$

The time average of the cross product $E_{x'}H_{y''}$, which can be measured in the satellite frame of reference, is

$$\langle E_{x'}H_{y'}\rangle = \tfrac{1}{2} E_o^2 \frac{n \cos \theta}{\mu_o c} \left[\frac{P}{P - n^2 \sin^2 \theta} \cos^2 \psi \right.$$

$$\left. + \left(\frac{D}{S - n^2} \right)^2 \sin^2 \psi + \Delta \right], \tag{3}$$

where

$$\Delta = \frac{-n^2 \cos \theta \sin \theta}{P - n^2 \sin^2 \theta} \frac{P \cos \psi}{P - n^2 \sin^2 \theta} \sin \delta_E$$

$$+ \left(\frac{D}{S - n^2} \right)^2 \sin \psi \tan \theta \sin \delta_B . \tag{4}$$

In obtaining Eq. (3) above, it has been assumed that $\cos \delta_E \simeq \cos \delta_B \simeq 1$. For small alignment errors, this is a good approximation. The error term Δ represents the deviation from magnetic alignment. For exact magnetic alignment, $\delta_E = \delta_B = 0$ and $\Delta = 0$.

Consider first the case of exact alignment. For $\Delta = 0$, the sign of $\langle S_z \rangle$ will be the same as the sign of $\langle E_{x'}H_{y'}\rangle$, independent of the unknown angle ψ, if the sign of the bracketed

term in Eq. (2) is positive. The sign of the bracketed term will be positive if $P < 0$. Since $P = 1 - f_{pe}^2/f^2$, this inequality is satisfied if the wave frequency f is less than the electron plasma frequency f_{pe}, a condition always satisfied at VLF frequencies for the Injun 5 orbit. Thus, for exact magnetic alignment, the direction of the Poynting flux for a single plane wave can be determined from the sign of the correlation $\langle E_x, B_y, \rangle$. It should be noted from Eq. (3) that only two field quantities, E_x, and H_y,, are necessary to determine the Poynting flux direction (up or down the geomagnetic field), whereas the z-component of the Poynting flux in Eq. (1) involves four field quantities: E_x, E_y, H_x, and H_y. However, the reduction from four to two field measurements in Eq. (3) has been made at the expense of a detailed knowledge of the Poynting vector, since one can only determine the direction of the Poynting flux along a field line from Eq. (3) and not the magnitude or absolute direction of the Poynting vector.

If a superposition of many waves is observed, then the above interpretation must be qualified. For multiple waves,

$$\langle \vec{S} \rangle = \langle \vec{E} \times \vec{H} \rangle = \langle \sum_i \vec{E}_i \times \sum_j \vec{H}_j \rangle ,$$

or
$$\langle \vec{S} \rangle = \sum_i \langle \vec{E}_i \times \vec{H}_i \rangle + \sum_{\substack{i,j \\ i \neq j}} \langle \vec{E}_i \times \vec{H}_j \rangle , \tag{5}$$

where the summations are over the individual waves. If these individual waves are uncorrelated, then the second summation in Eq. (5), for $i \neq j$, will be zero, yielding

$$\langle \vec{S} \rangle = \sum_i \langle \vec{E}_i \times \vec{H}_i \rangle \; .$$

Then

$$\langle S_z \rangle = \sum_i \langle E_{x_i} H_{y_i} - E_{y_i} H_{x_i} \rangle$$

$$= \sum_k \alpha_k(\theta) \, \langle E_{x_k'} H_{y_k'} \rangle \; . \tag{6}$$

Since the wave normal angles θ_k for the individual waves are in general different, the proportionality constants α_k will also be different for different waves, and the time average $\langle E_{x'} , B_{y'} \rangle$ for a superposition of many waves is not necessarily proportional to the average Poynting flux $\langle S_z \rangle$ of all the waves. In other words, a single proportionality constant cannot be substituted for the α_k and taken outside the summation in Eq. (6). Under these conditions the interpretation which can be made is as follows: if the sign of $\langle E_{x'} , B_{y'} \rangle$ is observed to be positive, then at least

some of the waves <u>must</u> have a Poynting flux in the positive z direction. However, there may also be waves with Poynting fluxes in the negative z direction and the relative intensity of these waves cannot be determined without further information .on the wave normal angles involved. Similar statements hold when the sign of $\langle E_x, B_y \rangle$ is negative. A measurement of $\langle E_x, B_y \rangle$ therefore allows one to make a positive statement that some waves are propagating in a certain direction, up or down the geomagnetic field; but it does not deny the possibility that there may be waves propagating in the opposite direction.

B. Discussion of Errors Due to Satellite Misalignment

The case of an alignment error will now be discussed. For non-zero Δ, the bracketed term in Eq. (3) will be positive if

$$\Delta/F > -1 , \tag{7}$$

where $F = \dfrac{P}{P - n^2 \sin^2 \theta} \cos^2 \psi + \left(\dfrac{D}{S - n^2}\right)^2 \sin^2 \psi .$

A measurement of the local plasma electron density and ion concentrations would permit the evaluation of P, S, and D, and n^2 in Δ and

F. However ψ and θ will be unknown quantities, which makes the evaluation of (7) for a specific case difficult. This problem can be avoided, however, by making a sufficient number of measurements. For given values of θ and ψ in (4), the sign of Δ will be determined by $\sin \delta_E$ and $\sin \delta_B$, each of which can be either positive or negative. Thus, there are four "error quadrants" in which the value of Δ/F must be investigated. However, there must always be at least one of these error quadrants in which Δ is positive and for which no error in the measurement can occur. Therefore, if a given type of phenomenon can be measured in all four error quadrants and the same result is obtained for each case, it may be concluded that the result is correct.

It is still desirable to understand the behavior of Δ/F in order to estimate the chances of making an error in any given measurement. This can be accomplished by examining Δ/F for certain special cases. Referring to (4), (7) can be written as

$$\left[\frac{n^2 \cos \theta \sin \theta}{P - n^2 \sin^2 \theta} \frac{\sin \delta_E}{\cos \psi} \right] \frac{\alpha}{\alpha + \beta} - \left[\tan \theta \frac{\sin \delta_B}{\sin \psi} \right] \frac{\beta}{\alpha + \beta} < 1 \tag{8}$$

where $\alpha = \dfrac{P}{P - n^2 \sin^2 \theta} \cos^2 \psi$

and $\beta = \left(\dfrac{D}{S - n^2} \right)^2 \sin^2 \psi$.

For the case of $\psi = \pi/2$, (8) becomes

$$-\tan \theta \sin \delta_B < 1 . \tag{9}$$

Since (9) is for a single plane wave, the worst case must be considered, that of $\tan \theta \sin \delta_B < 0$. It can be shown that (9) is satisfied for all wave normal angles θ less than $(\pi/2 - \delta_B)$.
In order to determine typical maximum misalignment errors, continuous Injun 5 magnetometer data from the on-board tape recorder were studied for several orbits during the month of January 1969. From revolutions 1907 through 1910, 355 minutes of continuous magnetometer data were examined and from revolutions 2077 through 2079, 337 minutes of data were examined. Typical maximum misalignment angles (the angle between the satellite x-axis and the geomagnetic field) for both of these periods were less than 10-12°, with a peak misalignment of 15° 25' for revolutions 1907 through 1910, and

18° 22' for revolutions 2077 through 2079. It should be noted that these large "peak misalignments" occur very infrequently, perhaps only once every 4-6 hours, with durations of only a few tens of seconds. In addition, it is expected that the misalignment will be slowly damped, becoming smaller with increasing time. Thus, since typical misalignment angles are less than 10-15°, no errors can be made at $\psi = \pi/2$ for wave normal angles less than about 75°, i.e., near-perpendicular propagation. This is what one would intuitively expect, since for perpendicular propagation, the wave magnetic field vector will lie in the plane of the magnetic loop antenna, and a displacement of the loop from this plane due to satellite misalignment could result in an error in the wave magnetic field measurement.

For the case of $\psi = 0$, (8) becomes

$$\frac{n^2 \cos \theta \sin \theta}{P - n^2 \sin^2 \theta} \sin \delta_E < 1 \ . \tag{10}$$

The worst case must again be considered, in which $\cos \theta \sin \theta \sin \delta_E < 0$. For $|P| > n^2$, (10) will always be

satisfied. Values of $|P|$ typically range from about 4×10^3 to greater than 10^7 for the Injun 5 orbit and n is generally of the order of 50 to 100. Thus, in general, $|P|$ will be greater than n^2. For $|P| < n^2$, (10) can be violated only for small θ ($\theta \leqslant \delta_E$). However, this corresponds to the physical situation of a very large refractive index at very small wave normal angles and cannot occur for whistler-mode waves below the electron gyrofrequency except at the ion gyrofrequencies. Thus, (10) will be satisfied for the Injun 5 orbit, with possible exceptions at the ion gyrofrequencies. Again, this is what one might intuitively expect, since the plane of rotation of the wave electric field vector will be nearly, though not exactly, perpendicular to the geomagnetic field vector. Thus, the plane of the wave electric field is unlikely to be perpendicular to the electric dipole antenna and, consequently, no error will occur in the wave electric field measurement.

For values of ψ between 0 and $\pi/2$, (8) is merely a weighted sum of the terms discussed above from (9) and (10). Thus, (9) and (10) may be thought of as worst cases for the behavior of Δ/F and indicate that errors in the Poynting flux measurement can occur only for waves propagating nearly perpendicular to the geomagnetic field.

C. The Poynting Flux Measurement Technique

The coordinate system used for the above Poynting flux derivations and illustrated in Fig. 2 was chosen to correspond with that commonly used in the plasma literature; it is not the same as that used on the Injun 5 satellite, where the satellite is aligned with the positive x-axis along the geomagnetic field (see Fig. 1). However, it is easily seen that, through a permutation of coordinate axes, the measurement of the sign of $\langle E_y B_z \rangle$, where y and z are now in the Injun 5 frame of reference, is sufficient to determine the direction of the Poynting flux along the geomagnetic field (x-axis).

The actual correlation measurements are made on the ground using the wide-band analog electric and magnetic field signals transmitted from the satellite. These wide-band signals are filtered by an Ad-Yu Electronics Model 1034 Dual Channel Synchronous Filter to select the frequency at which the correlation of the two signals is to be determined (see Fig. 3). The pass bands of the two narrow-band filter channels are closely matched, the center frequency of the two filter channels being determined by a single tuning oscillator and the bandwidth by plug-in units. A bandwidth of 50 Hz has been used for all measurements presented in this thesis. The two narrow-band outputs from the synchronous

filter then go to a four-quadrant analog multiplier which produces an output proportional to the algebraic product, $E_y B_z$, of the narrow-band E_y and B_z input signals. The analog multiplier output is then averaged by a simple R-C integrator with an R-C time constant of 50 milliseconds to give a good approximation to the time averaged product $\langle E_y B_z \rangle$.

In the process of transmitting and demodulating the wide-band electric and magnetic field signals, various frequency-dependent phase shifts occur which must be corrected with a phase shift network prior to making a correlation measurement. (The results of the prelaunch phase calibrations are presented and discussed in the appendix.) Based on the reproducability of the prelaunch calibrations, the overall uncertainty in the phase shift corrections required is believed to be less than ± five degrees. To establish that errors of this magnitude do not affect the sign of the correlation measurement, it has been required for all data presented that a phase shift of ± ten degrees applied to one channel not change the sign of the correlation measurement. In most of the data, much larger phase shifts have been applied to ascertain that such errors are not affecting the measurement.

The determination of the Poynting flux direction of proton whistlers provides a good check on the Poynting flux sensing technique, since proton whistlers (at higher latitudes) are known

to be propagating _upward_ from the base of the ionosphere [see Gurnett et al., 1965]. Figure 4 illustrates the determination of the Poynting flux direction for a series of proton whistlers. The Poynting flux is observed to be directed upward as expected. Identical results have been obtained from the observations of proton whistlers in approximately 50 additional Injun 5 revolutions. It should be noted here that $\langle E_y B_z \rangle$ differs from a correlation coefficient in that it is not normalized; hence the correlation levels for the various proton whistlers in Fig. 4 depend on the intensity of the proton whistler signals.

In order to further ascertain that the measurement is performing properly, the Poynting flux has been determined for short fractional-hop whistlers (which are known to be propagating up the geomagnetic field from below the ionosphere) from approximately 150 Injun 5 revolutions. In all cases, the short fractional-hop whistlers were observed to be upgoing. In addition, downgoing long-hop whistlers are often observed following the short-fractional-hop whistlers, providing further support for the accuracy of the Poynting flux measurement technique.

III. THE RESULTS OF THE MEASUREMENTS OF THE POYNTING FLUX DIRECTION FOR VLF WAVES IN THE MAGNETOSPHERE

A. Description of the Data

The Injun 5 data presented in this thesis was acquired by the North Liberty Data Acquisition Facility of the University of Iowa during the periods 31 December 1968 through 25 February 1969 and 4 March 1969 through 12 May 1969. Of the 1529 Injun 5 revolutions during these periods, VLF data were acquired for 628 revolutions and data for the Poynting flux measurements was obtained from the study of 329 revolutions. These 329 revolutions give a good sampling of magnetic local time (MLT) and Injun 5 altitudes and are distributed throughout the December through May time period. The data cover the range of invariant latitudes (INVL) from approximately 35° to 75°. (MLT is the hour angle between the magnetic meridian through the satellite and the magnetic meridian through the sun, and INVL is arccos $L^{-\frac{1}{2}}$, where L is McIlwain's [1961] geomagnetic shell parameter.)

The principle object of the data analysis program was to determine the Poynting flux direction for as many different types of VLF emission and propagation phenomena as possible, rather than to make statistical studies of any particular emission type.

Detailed studies of some types of emissions were required, however, necessitating a concentration of data in certain magnetic local time and altitude ranges. The results of the Poynting flux measurements are presented below and are classified by the type of emission or propagation phenomena.

B. Reflection Phenomena

The determination of the Poynting flux by the methods described above is an especially good tool for the study of reflection phenomena. Figure 5 illustrates some discrete VLF emissions occurring in pairs, the two components of each pair being separated by a few tenths of a second. The correlation measurement clearly shows that the first emission in each pair is downgoing and that the second emission is upgoing, indicating that the emissions have been reflected below the satellite altitude of approximately 1350 km. (The two intense, discrete tones occurring from 0140:15 to 0140:23 UT are from the electric antenna impedance measurement.) The dispersion of the emission gives further evidence of a reflection, the time delay between the two components of each pair being greater at lower frequencies. These delay times are consistent with a reflection at the base of the ionosphere below the satellite.

C.   Subprotonospheric Whistlers

Illustrated in Fig. 6 is an example of short fractional hop whistlers followed by a subprotonospheric (SP) whistler at an altitude of 720 km.   The correlation measurement indicates that the short fractional hop whistlers are upgoing, followed by the alternate downgoing and upgoing hops of the SP whistler (the second hop of the SP whistler was apparently not intense enough at the correlation frequency to obtain a correlation). The second through the fifth SP whistler traces in the electric and magnetic receiver spectrograms in Fig. 6 each consist of two traces, the first one upgoing and the second one downgoing, and are resolved by the correlation measurement.

SP whistlers were first reported by Carpenter et al. [1964] and were explained by Smith [1964] in terms of multiple reflections between the lower ionosphere and a region around 1000 km.   The reflection at low altitudes is due to periodic latitudinal gradients of the electron density in the lower ionosphere; the mechanism at the higher altitude involves a refraction of the wave through the transverse region of propagation at the base of the protonosphere, the region where hydrogen ions begin to predominate [Smith, 1964].

The close spacing in time of upgoing and subsequent down-going waves in Fig. 6 indicates that the satellite was very near

the upper reflection altitude of the SP whistler. This is in agreement with the above theory since the protonosphere should decrease in altitude during local night, when the observation in Fig. 6 was made.

D. Periodic Emissions

Figures 7 and 8 illustrate examples of periodic emissions in which all of the observed emissions are downgoing. For the non-dispersive periodic emission shown in Fig. 7, in which there is little or no observable systematic change in period with frequency, it is believed that an emission is triggered by another emission propagating in the whistler mode. If this triggered emission propagates to the conjugate hemisphere in the whistler mode at the appropriate frequency, then the triggering process is repeated, giving rise to a set of periodic emissions in which the period is equal to the whistler mode group delay at the triggering frequency. Such a process requires strong absorption of the whistler mode echo, coupled with strong emission in the triggering process [Helliwell, 1965]. On the other hand, weak absorption and weak emission will give rise to dispersive periodic emission in which there is a systematic variation with frequency of the period between the bursts. This type of emission is shown in Fig. 8.

The emissions illustrated in Fig. 7 were observed for a
period of three minutes over an altitude range of approximately
150 km and a range of magnetic shell parameters from L = 4.2 to
L = 3.6. Since the echo period is very nearly constant over this
large range of L values, it is concluded that the echoing must be
very strongly guided by the geomagnetic field but that the observed
emissions must have "leaked" from the L-shell on which the echoing
is taking place and propagated directly to the satellite. The
observation in Fig. 7 strongly supports this conclusion since no
upgoing waves associated with this echoing process are observed.

The same conclusions may be drawn from the dispersive
periodic emissions in Fig. 8. Although these emissions were
observed for a much shorter time period than those of Fig. 7,
the echo period is again very nearly constant and only downgoing
waves are observed. At 1225:30 UT in Fig. 8, there is a single
burst of upgoing noise which appears to be an echo or reflection
of a burst which occurred a few tenths of a second before. This
does not appear to be associated with the periodic emissions but
rather seems to be a discrete burst of noise which may have been
reflected in the lower ionosphere and propagated back to the
satellite.

E. ELF Hiss

1. Results of Observations

Illustrated in Fig. 9 is an example of a magnetospheric radio phenomenon called ELF hiss [Gurnett, 1968] observed at an altitude of approximately 1200 km. From the correlation measurement at 600 Hz, the ELF hiss is clearly downgoing. Figure 9 also illustrates a correlation measurement at the sharp lower cutoff frequency (510 Hz) of the ELF hiss band. In this measurement, both downgoing and upgoing waves are observed with the upgoing component being less intense, indicating that reflections of the ELF hiss are occurring below the satellite. These observations are consistent with the explanation of the low-frequency cutoff of ELF hiss given by Gurnett and Burns [1968] in terms of reflections near the two-ion cutoff frequency and will be discussed in the next section.

Figure 10 illustrates another example of ELF hiss at an altitude of approximately 2500 km which is upgoing until 1418 UT and downgoing after 1419 UT. In order to further investigate this phenomenon of upgoing ELF hiss, a detailed study of ELF hiss correlation measurements from 140 Injun 5 revolutions was made. These measurements extended over the entire Injun 5 altitude range, from 35° to 75° INVL (a single observation was made between 80° and 90° INVL), and for most magnetic local times.

The results of these measurements are presented in Figs. 11 and 12. In Fig. 11, the Injun 5 orbit is plotted, in altitude versus invariant latitude, for all times at which downgoing ELF hiss was observed. Figure 12 is a similar plot for upgoing ELF hiss. As can be seen from these plots, downgoing ELF hiss was observed over the entire region of altitude-invariant latitude space under study, whereas the highest latitude at which upgoing ELF hiss was observed is approximately 60° INVL. Furthermore, with the exception of three isolated observations of less than one minute duration, all observed cases of upgoing ELF hiss below 1500 km occurred at local night, between 18:00 and 6:00 hours MLT.

Since the high-latitude cutoff for upgoing ELF hiss coincides with the approximate location of the plasmapause boundary [Carpenter, 1966], data from the AFCRL electron density probe on Injun 5 were examined for 16 cases in which a transition between downgoing and upgoing ELF hiss was observed. In five of these cases, the transition occurred on the low-latitude side of the plasmapause boundary, within the plasmasphere. In the remaining 11 cases, the transition occurred within the plasmapause boundary, in the region of the "knee" in the electron density profile. A typical example of this transition within

the plasmapause boundary is illustrated in Fig. 10. After a slight peak in electron density at 1414:30 UT, N_e begins to decrease with the largest gradient occurring between 1417:30 and 1418 UT, at approximately 56.5° INVL (L = 3.3). The transition from upgoing to downgoing ELF hiss occurs at 1418:30 UT at all frequencies at which the emission is observed. The correlation measurement at 250 Hz in Fig. 10 intercepts the lower frequency cutoff of the ELF hiss (visible in the low-band electric and magnetic receiver data) at 1413:30 UT. In this measurement, only upgoing waves are observed, in contrast to the correlation measurement at the lower frequency cutoff in Fig. 9, where both downgoing and upgoing waves were observed.

Two other features are often present in the high-band electric receiver data at plasmapause crossings and can be seen in Fig. 10. First, a breakup in the lower hybrid resonance (LHR) noise band begins at 1417:40 UT, with the noise continuing until approximately 1420 UT. The LHR breakup at the plasmapause has been identified and discussed by Carpenter et al. [1968]. Secondly, the electric antenna impedance increases sharply between 1418:30 and 1419 UT. Since the impedance is a function of both the electron density and the electron temperature, it must be concluded that either the density or temperature, or both,

undergo a rather discontinuous change at this time. The plot of N_e versus time in Fig. 10 does not reflect this feature since the electron density calibration is a function of electron temperature and spacecraft potential, neither of which were available at the time these preliminary electron density data were prepared. For the plot in Fig. 10, a constant temperature and potential were assumed. Nevertheless, this simplification can only affect the magnitude of the "knee" but not its general location or features.

As a check on the validity of the transition between upgoing and downgoing hiss, large phase shifts were introduced in both the electric and magnetic signals prior to making the correlation measurement for a large number of cases in which a transition occurred. Since this transition often occurs at very nearly the same time that a large change in the electric antenna impedence is observed (see Fig. 10), it might be argued that the observed transition in propagation direction is an instrumental effect caused by the high electric antenna impedance. However, in all of the cases checked, very large phase shifts were required to change the sign of the correlation measurement for both downgoing and upgoing hiss. In addition, in a large number of observations of ELF hiss, short-fractional-hop whistlers were observed simultaneously and were

always found to be upgoing, as expected. Whenever short-fractional-hop whistlers were simultaneously observed on both sides of a transition between upgoing and downgoing hiss, identical phase shifts were required to change the signs of both the ELF hiss correlation and the whistler correlation measurements, giving very good evidence that the change in the propagation direction of ELF hiss as determined by the Poynting flux measurement is indeed a real effect. It is therefore concluded that large electric antenna impedances are not affecting the correlation measurements of ELF hiss.

No systematic dependence of the correlation measurements on the satellite orientation has been observed for any of the ELF hiss cases studied and it is concluded that errors in the magnetic alignment of the satellite did not affect the Poynting flux determinations for ELF hiss.

2. Interpretation of Results

The observations of downgoing ELF hiss over the entire range of altitude and invariant latitude under study is in agreement with previous evidence on the direction of propagation of ELF hiss. Kennel and Petschek [1966] suggested that the generation of VLF whistler-mode noise at high altitudes near the equatorial plane might account for the wave energy necessary to drive observed pitch-angle diffusion, resulting in particle precipitation into the ionosphere. Russell et al. [1969] have observed the occurrence of steady ELF noise in the region below $L = 6$ from 0.00 to 6.00 MLT and at magnetic latitudes around $45°$ above $L = 6$ in the sunward hemisphere.

Gurnett and Burns [1968] explained the sharp lower cutoff frequency of ELF hiss in the ionosphere in terms of the reflection of downward-propagating waves near the two-ion cutoff frequency between the proton and helium gyrofrequencies. The correlation measurement at the lower frequency cutoff illustrated in Fig. 9 provides the first direct experimental evidence to support the reflection mechanism proposed by Gurnett and Burns. The correlation at 510 Hz in Fig. 9 indicates that reflections of downgoing waves are occurring near the two-ion cutoff frequency. However, the correlation measurement at 600 Hz, showing only

downgoing waves, suggests that the ELF hiss is not being reflected below the satellite altitude at this frequency. This can occur if the wave frequency is above the maximum two-ion cutoff frequency in the ionosphere at all altitudes below the satellite. The two-ion cutoff is seldom observed above 600-650 Hz [Gurnett and Burns, 1968] so that the ELF hiss at 600 Hz in Fig. 9 is very likely above the maximum two-ion cutoff and is, therefore, able to propagate to the base of the ionosphere, where strong absorption can occur to attenuate the reflected wave.

The observations of upgoing ELF hiss can be explained in terms of a propagation effect in which downgoing waves may propagate across the plasmapause to lower latitudes and be subsequently refracted upwards and trapped within the plasmasphere. This explanation is able to account for (1) the high-latitude cutoff of upgoing ELF hiss, (2) the decrease, during local night, of the minimum altitude at which upgoing ELF hiss is observed, and (3) the observation of upgoing ELF hiss with a low-frequency cutoff (see Fig. 10).

In order to examine the propagation effects responsible for the observations of upgoing ELF hiss in the plasmasphere, consider a wave propagating down the geomagnetic field in the low-density region on the high-latitude side of the plasmapause

boundary. The refractive index surface for this wave is shown in Fig. 13(c). Also shown in Fig. 13 is a plot of the perpendicular refractive index $n_\perp$ versus altitude in the plasmasphere (Fig. 13(a)) and a plot of the electron density N_e versus latitude at the plasmapause (Fig. 13(b)). If the downgoing wave is not propagating exactly parallel ($\theta = 0$) to the geomagnetic field, then it can propagate across field lines to lower latitudes, thereby crossing the plasmapause boundary and entering a region of higher density. The density increase at the "knee" may be as much as a factor of 10 to 20. As the wave propagates into the higher density region, $n_\parallel$ will remain nearly constant across the horizontal gradient (see Fig. 13(c)). However, $n_\perp$ will increase with increasing electron density, thereby increasing the wave normal angle θ. Since θ is still less than $\pi/2$, the wave will continue to propagate downward. If, however, the wave is above the altitude at which $n_\perp$ in the plasmasphere is a minimum, $n_\perp$ will decrease as the wave propagates downward, causing θ to finally become equal to $\pi/2$. At this point, $n_\perp$ can no longer decrease and the wave will refract upwards ($\theta > \pi/2$). On the other hand, if the wave is at an altitude below the minimum in $n_\perp$ when it crosses the plasmapause boundary, then the wave will be able to propagate into the lower ionosphere.

In order to investigate the behavior of $n_\perp$ as a function of altitude, $n_\perp$ was calculated in a computer program using several different ionospheric models computed by Colin and Dufour [1968] for solar minimum conditions. These models provide a suitable indication of the behavior of $n_\perp$ as functions of both altitude and local time. For daytime ionospheric models at solar minimum, the minimum in $n_\perp$ ranges from approximately 1500 km to above 3000 km. For nighttime models, however, this minimum can decrease by a factor of two to three, to well below 1000 km. Thus, the propagation model described above can account for the fact that upgoing ELF hiss is observed below 1500 km only during local night. In addition, the ionospheric model programs indicated that there was no substantial dependence of the minimum $n_\perp$ altitude upon frequency over the frequency range of ELF hiss. This is in agreement with the observations which show that the transition between upgoing and downgoing waves occurs at very nearly the same time at all frequencies (see Fig. 10).

In order to explain the lower frequency cutoff of upgoing ELF hiss in the plasmasphere, consider again a wave propagating down the geomagnetic field just outside the plasmapause boundary. The two-ion cutoff frequency in this region will decrease with increasing altitude. At some given altitude h^*, only waves with

frequencies greater than or equal to the local two-ion cutoff frequency f^* may be observed; all waves with frequencies less than f^* will have been reflected, outside the plasmasphere, at altitudes greater than h^*. The waves with frequencies greater than f^* which are able to propagate to altitudes below h^* may cross the plasmapause boundary and be refracted upwards, as discussed above. If the satellite is at or near the altitude h^*, within the plasmasphere, these upgoing waves will be observed at the satellite. However, upgoing waves at frequencies less than f^* will not be observed at the satellite since they are not able to enter the plasmasphere below the satellite. Thus, a lower frequency cutoff of upgoing waves will be observed. But this cutoff will be near the two-ion cutoff frequency at altitude h^* outside the plasmasphere, rather than near the local two-ion cutoff frequency at the satellite as discussed by Gurnett and Burns [1968].

The absence of downgoing waves at the lower cutoff frequency in Fig. 10 suggests that either (1) all waves which enter the plasmasphere above altitude h^* are refracted before they reach the satellite, or (2) no waves enter the plasmasphere above altitude h^*. The latter might occur if, for example, the wave normal angles have not deviated sufficiently from $\theta = 0$ (parallel

propagation) in order to propagate across field lines and into the plasmasphere by the time they reach altitude h^*.

It should be pointed out here that the reflection of down-going ELF hiss in the lower ionosphere might provide an additional source for upgoing waves within the plasmasphere. It has been suggested by Heyborne et al. [1969] that the observed cutoff of VLF signals beyond the plasmapause in the ionosphere might be due to a sharp increase in absorption in the lower ionosphere beyond the plasmapause. Such an absorption increase could explain the absence of upgoing waves outside the plasmasphere while allowing reflected waves to propagate upward within the plasmasphere. Such a mechanism, however, cannot account for the diurnal variation of the minimum altitude at which upgoing waves are observed in the plasmasphere. It is therefore concluded that such reflections in the lower ionosphere can only contribute in small part, if at all, to the observed behavior of ELF hiss propagation. Similarly, a source of ELF hiss at low altitudes in the plasmasphere (in addition to sources at high altitudes) might successfully explain the observations of upgoing waves in the plasmasphere. However, such a mechanism cannot explain the observation of upgoing hiss with a low-frequency cutoff.

Once a wave is within the plasmasphere, it is not a simple matter for it to propagate across the plasmapause boundary to the low density region. Conditions of total internal reflection could result in a trapping of waves, and consequently, energy, within the plasmasphere. Under these conditions, one would expect to observe higher intensities of ELF emissions within the plasmasphere than without. It is proposed that this trapping of waves within the plasmasphere can account for the observations of much greater ELF hiss intensities below L values of 4 to 6 than at higher L values by Russell et al. [1969], using OGO-3 data. It is further suggested that ELF hiss which is observed within the plasmasphere might possibly be due to sources outside the plasmasphere.

F. Chorus

Illustrated in Figs. 14 and 15 are examples of VLF chorus at an altitude of 2530 km. The correlation in Fig. 14 shows the chorus to be downgoing at 69.9° INVL and in Fig. 15 shows the chorus to be upgoing at 51.4° INVL. The results of these and 15 additional measurements all indicate that chorus is propagating down the geomagnetic field lines from sources at altitudes above the satellite and that upgoing chorus occurs only within the plasmasphere, just as for ELF hiss.

The observations of downgoing chorus presented here are in apparent disagreement with the theory proposed by Swift [1968] in which chorus is generated at low altitudes by an electrostatic loss-cone instability associated with ring current protons. The observations of Russell et al. [1969] are in agreement with the observations described here as concerns the source altitude for chorus. However, a comparison of the same data raises a question concerning chorus propagation. Russell et al. [1969] observed an increase in the frequency of occurrence of chorus at high altitudes for L-values above 7 but observed chorus infrequently for L-values less than 5. Since chorus occurs in the same frequency range as ELF hiss and is propagating in the same mode, then one would expect a trapping of waves in the plasmasphere in the same manner as for ELF hiss; the Injun 5 observations would support such a result. However, the results of Russell et al. [1969] are inconsistent with such a process. In addition, Burtis and Helliwell [1969] find that banded chorus is also most common outside the plasmapause in the equatorial region.

In order to resolve this inconsistency and to gain a better understanding of the propagation of chorus, additional examples must be studied using the Poynting flux measurement technique.

G. VLF Hiss

1. Results of Observations

Figures 16 through 21 illustrate correlation measurements for VLF hiss. In these six examples, and in 34 additional examples which have been studied, VLF hiss is observed to be propagating down the geomagnetic field lines. In addition, in all but 5 of the 40 cases studied, there are also waves propagating up the geomagnetic field from below the satellite. The upgoing waves are much less intense than the downgoing waves and the impulsive bursts which characterize many of the VLF hiss events are much less frequent for the upgoing waves than for the downgoing waves.

Several distinct spectral forms of VLF hiss have been found in the Injun 5 data, including two types which have not been previously distinguished. Figure 16 illustrates the most commonly-observed form of auroral-zone VLF hiss. This type of hiss has been discussed in detail by Gurnett [1966], who referred to it as impulsive hiss, and is characterized by slow spectral variations on a time scale of the order of a second and a lower cut-off frequency that tends initially to decrease with increasing latitude, reaching a minimum at about 70° INVL, and then tends to increase with increasing latitude [Gurnett, 1966]. This latitudinal frequency dependence is dramatically illustrated in

Fig. 17, which shows a transition between impulsive VLF hiss and a smoother form of hiss. The hiss occurring after 2339 UT in Fig. 17 is one of the few cases studied in which only downgoing waves were observed.

Figures 18 and 19 illustrate two types of V-shaped VLF hiss. This type of emission was first discussed by Gurnett [1966], who found that V-shaped hiss often occurred in association with intense fluxes of 10 keV precipitating electrons, using Injun 3 data. V-shaped hiss is characterized by narrow bands of emission which exhibit a smooth, steady variation of frequency with time. It may be symmetric in shape, as in Fig. 18, from which the "V-shaped" name is derived, or it may merely consist of segments of narrow emission bands, as in Fig. 19. V-shaped hiss is often accompanied by a diffuse background of relatively weak VLF hiss.

The type of emission illustrated in Fig. 20 has not been previously reported and, although similar to V-shaped hiss, is unusual in that the bands are very intense and well defined and the wave magnetic field is very weak. (Although not visible in the spectrogram, the high sensitivity of the correlation measurement enables the wave magnetic field to be detected.)

Illustrated in Fig. 21 is a new type of VLF hiss which occurs commonly at sub-auroral latitudes and which is called

mid-latitude hiss. It is characterized by a narrow band of emission, of the order of 1-2 kHz in width, and exhibits a small latitudinal frequency dependence, the frequency decreasing with increasing latitude. Mid-latitude hiss has not been observed above 65° INVL on Injun 5, whereas auroral-zone VLF hiss is seldom observed at latitudes below 65° INVL [Gurnett, 1966].

VLF hiss has been observed in all four of the "error quadrants" discussed in Chapter II and no orientation dependence has been observed. It is concluded, therefore, that the misorientation of the satellite is also not affecting the Poynting flux determinations of VLF hiss.

2. Discussion of Results

The observations of downgoing VLF hiss clearly indicate that VLF hiss is generated above the altitude range of the Injun 5 satellite. The simultaneous observations of upgoing VLF hiss may be due to the reflection of downgoing waves below the satellite, or additional emission of VLF hiss below the satellite, or a combination of the two. It will be suggested below that the results of the Poynting flux measurements of VLF hiss are consistent with (1) emission by Cerenkov, and possibly cyclotron, radiation and (2) a reflection of downgoing VLF hiss below the altitude at which the wave frequency is equal to the local LHR frequency. A tentative

explanation of mid-latitude hiss is suggested and possible mech-
anisms for the generation of V-shaped hiss are discussed.

Liemohn [1965] and Mansfield [1967] have treated the problem
of the radiation from a charged particle spiraling in a magneto-
plasma. They discuss three types of emission which may propagate
in the whistler mode at very low frequencies: Cerenkov radiation,
"normal" cyclotron radiation, and "anomolous" cyclotron radiation.
Cerenkov radiation is emitted entirely in the forward hemisphere
with respect to the guiding center motion of the particle and is
produced by the charge's polarization field through constructive
interference when the local phase velocity is less than the par-
ticle velocity. Doppler-shifted cyclotron radiation is produced
by the acceleration due to the orbit gyrations of the particle,
and consists of a "normal" emission in which the particle moves
slower than the local phase velocity and which is emitted entirely
into the backward hemisphere in the whistler mode, and an
"anomolous" emission in which the particle moves faster than the
local phase velocity and which is emitted entirely into the for-
ward hemisphere [Liemohn, 1965]. Liemohn [1965] concluded that
the total energy produced by an incoherent Cerenkov radiation
process was too low to explain the observed power densities of
VLF hiss. However, Jørgensen [1968] showed that Liemohn's [1965]

total power calculations were several orders of magnitude too low,
thereby reopening the possibility that auroral-zone VLF hiss can
be generated by incoherent Cerenkov radiation.

There is insufficient data available at present to estimate
the contribution of "normal" cyclotron radiation to VLF hiss
emission. Such radiation would be emitted in the backward hemi-
sphere from the particle motion and thus particles precipitating
down the geomagnetic field might account for the observation of
upgoing, as well as downgoing, VLF hiss. If emission does occur
both above and below the satellite, it would be reasonable to
expect higher intensities from downgoing waves than from upgoing
waves, since there is a much greater flux tube volume in which
radiation can be generated above the satellite than below. Higher
downgoing wave intensities are, in fact, observed in the Injun 5
Poynting flux measurements.

In addition to the possibility of emission below the satel-
lite, it is expected that reflections of downgoing waves below the
satellite will contribute to the upgoing component of VLF hiss.
Such reflections will most likely occur near the altitude at which
the wave frequency is equal to the local LHR frequency, since the
lower hybrid resonance is the only resonance or cutoff in the
refractive index in the frequency range of VLF hiss observed with

Injun 5. The reflection mechanism at the LHR frequency has been discussed by Thorne and Kennel [1967] and by Storey and Cerisier [1968], who show that downgoing waves with wave normal angles near $\pi/2$ will be reflected when the local LHR frequency exceeds the wave frequency.

A Cerenkov radiation mechanism might also provide a plausible explanation for the mid-latitude hiss observations, as illustrated in Fig. 21. The power radiated by Cerenkov emission is very strongly peaked at the local LHR frequency with much larger powers emitted above the LHR frequency than below [Jørgensen, 1968]. Thus, at lower latitudes where much smaller precipitating particle fluxes are available, one would expect intense emission to occur only over a narrow band of frequencies near the local LHR frequency. Due to the altitude dependence of the LHR frequency, the frequency of most intense emission will increase as a radiating particle travels down a field line from high altitudes. However, since the emission will be generated near the local LHR frequency with large wave normal angles, the downgoing waves will be reflected soon after the LHR frequency exceeds the wave frequency. Thus, intense emission would be observed from the region just above the satellite and would occur near the local LHR frequency. The frequency of the "band" of mid-latitude hiss illustrated in Fig. 21 is consistent

with determinations of the local LHR frequency at these latitudes
with the Injun 5 VLF experiment [R. R. Anderson, personal communi-
cation].

Since the V-shaped hiss events are often found in associa-
tion with intense fluxes of precipitating particles [Gurnett, 1966],
and since the correlation measurements of V-shaped hiss events
yield similar results to the measurements of normal VLF hiss, it
is suggested that the same emission mechanism(s) may be responsible
for the V-shaped hiss events. The characteristic shape might be
produced by (1) a frequency-dependent limiting ray angle for
propagation from the source to the satellite, or (2) some form
of resonance effect in which a source radiates at different fre-
quencies as it propagates down the geomagnetic field. The examples
illustrated in Figs. 18 and 19 are suggestive of an explanation
in terms of the first hypothesis, since the V-shaped emissions
seem to be "filled-in" as might happen if a source radiates con-
tinuously along a field line, whereas the example illustrated in
Fig. 20 is suggestive of the second hypothesis, since it is
difficult to understand how a source could radiate continuously
at all frequencies and generate the extremely sharp spectral form
of Fig. 20. An explanation in terms of a limiting ray angle for
propagation is discussed in detail in the next section for

saucer-shaped emissions, which are generated below the satellite altitude, and will not be discussed here. It is possible that such a propagation effect could also explain the V-shaped hiss events generated above the satellite altitude. Such an explanation is further suggested by the fact that V-shaped hiss events often have very weak magnetic fields, indicating that propagation with large wave-normal angles may be occurring, just as for the saucer-shaped emissions. In order for an explanation of the V-shaped hiss events to be satisfactory, however, it must also be able to account for the simultaneous generation of the rather diffuse, low intensity background hiss, as well as the intense, sharply-defined V-shaped emissions.

In summary, it is suggested that the Poynting flux measurements of VLF hiss are consistent with radiation from precipitating particles (at altitudes up to several earth radii) by a Cerenkov, and possibly a cyclotron, mechanism. In addition, it is expected that the reflection of downgoing waves below the altitude at which the wave frequency is equal to the local LHR frequency can explain some, if not all, of the upgoing VLF hiss observed with Injun 5.

H. Saucer-Shaped Emissions

1. Results of Observations

Illustrated in Figs. 22 through 24 are examples of a new type of emission which is called a "saucer", following the terminology of several investigators. In each of six examples investigated to date, the Poynting flux of the saucer-shaped emission is directed up the geomagnetic field line, indicating that the source of the emission may be below the satellite. The six examples studied ranged in altitude from 1840 to 2530 km and in latitude from 69.4° to 74.5°, indicating that the saucer-shaped emission is predominately an auroral-zone phenomenon. Correlation measurements for saucer-shaped emissions have been performed in each of the four "error quadrants" of satellite misalignment (see Chapter II) and no orientation dependence has been observed in the measurement.

Saucer-shaped emissions were first observed with the Alouette 1 and 2 satellites. They typically have a duration of from one second to several tens of seconds and occur in the frequency range from about 2 kHz to above 10 kHz. The outer "envelope" of the emission is often sharply defined, as for the case shown in Fig. 22, and the electric field intensity is usually greater than the magnetic field intensity, relative to free space. Within the outer

envelope of the saucer, the emission may be rather diffuse, tending
to partially "fill in" the characteristic parabola or hyperbola
shape, as in Fig. 23, or the saucer may be a very distinct and
well-defined line, as in the emissions in Fig. 24. Figure 24 is
a good example of multiple saucer-shaped emissions and indicates
that several saucers, each having different width, may be super-
imposed in time. The saucer-shaped emissions are not always
symmetric in time; sharp changes in intensity may occur, as well
as frequency shifts from one half to the other, as illustrated
in Fig. 23, and gaps may occur at the minimum frequency of emission.
In addition, spectrograms of these emissions sometimes have atten-
uation bands at harmonics of the proton gyrofrequency (see Fig. 14
of Gurnett et al. [1969]).

As a result of the Poynting flux measurements of saucer-
shaped emissions, they are considered to be distinctly different
from the V-shaped hiss events, although they may possibly be
generated by the same type of emission mechanism. The symmetry
of the saucer envelope suggests that the source of this emission
may lie along the symmetry axis of the emission, i.e., on the
magnetic field line passing through the satellite at the time
the minimum frequency is observed, much as for the V-shaped
hiss events. Unfortunately, because of the limited number of

saucer observations in the Injun 5 data to date, the relationship between the saucer-shaped emissions and charged particle fluxes has not yet been investigated.

2. A Qualitative Explanation of the Saucer Envelope

(NOTE: The following discussion and explanation of the saucer envelope is from Mosier and Gurnett [1969] and was evolved jointly with D. A. Gurnett.)

When the anisotropic propagation of whistler-mode waves upward from a source below the satellite is considered, a ready explanation arises for the characteristic frequency-time spectra of the saucer-shaped emissions. For a qualitative model, the source is assumed to be of small extent in the north-south direction, such as a point source or a source distributed along an east-west line (an auroral arc, for example), and located below the satellite. The sharply defined frequency-time envelope of the saucer can then be explained by a frequency-dependent limiting ray angle for propagation from the source to the satellite. The noise intensity variations observed at a given frequency are then completely due to the horizontal (north-south) motion of the satellite through the "beam" of allowed ray paths from the source to the satellite, and the frequency dependence of the beam width accounts for the observed frequency-time envelope of the emission.

For the whistler mode of propagation there are two limiting ray angles which could possibly explain the observed beam width. As shown by Smith [1960], Helliwell [1965], and others, the angle ψ between the ray direction and the static magnetic field depends on the wave normal angle θ, also measured relative to the static magnetic field, as shown in Fig. 25(a). (This angle ψ should not be confused with the azimuthal satellite orientation angle ψ used in Chapter II.) The first limiting ray angle, ψ_{max}, occurs at a wave normal angle intermediate between $\theta = 0$ and $\theta = \theta_{res}$. This first limiting ray angle was originally discussed by Storey [1953] in connection with the guiding of whistlers in the geomagnetic field. In the low frequency limit ψ_{max} is approximately 19° 29' [Storey, 1953]. The second limiting ray angle, ψ_{res}, occurs as the refractive index goes to infinity at a wave normal angle equal to the resonance cone angle, θ_{res}. Since the ray direction is perpendicular to the refractive index surface [Stix, 1962], the simple geometric construction in Fig. 10(b) shows that

$\psi_{res} = \pi/2 - \theta_{res}.$

Several factors strongly suggest that it is this second limiting ray angle, ψ_{res}, for wave normal angles near the resonance cone angle, which accounts for the characteristic shape of the saucer envelope:

(1) Since the temporal (spatial) width of the envelope increases
with increasing frequency, the limiting ray angle <u>must</u> in-
crease with increasing frequency. Only ψ_{res} has the required
frequency dependence since ψ_{max} decreases with increasing
frequency [see Smith, 1960].

(2) The large observed ratio of electric-to-magnetic field
strengths for the saucer-shaped emissions suggests that
the wave normal angle is very close to the resonance cone
angle.

(3) The proton cyclotron harmonic interaction observed and the
doppler shifting of the cyclotron harmonic frequencies
sometimes observed [Gurnett et al., 1969] suggest that the
wavelengths involved may be as short as 100 meters, corres-
ponding to a very large refractive index ($\sim$ 300). These
very short wavelengths are possible only for wave normal
angles near the resonance cone angle.

Wave normal angles very near the resonance cone angle could

occur because of several possible reasons. The emission mechanism

may favor the production of waves with wave normal angles near the

resonance cone angle. Also, even for wave normal angles not

initially near the resonance cone angle the rapid decrease in the

electron density and refractive index with increasing altitude by

Snell's law causes the wave normal angle to approach the resonance cone angle as the wave propagates upward through the ionosphere.

The qualitative explanation of the frequency-time shape of the saucer-shaped emission is illustrated in Figs. 25(c) and 25(d) which show the limiting ray paths from the source to the satellite at several frequencies and the resulting frequency-time spectrogram observed by the satellite passing over the source. For this qualitative illustration, it is assumed that the plasma parameters are independent of altitude so that the ray paths are straight lines. A more quantitative model would of course require a detailed ray path integration.

The simple ray path model illustrated in Fig. 25 qualitatively explains the principal feature of the saucer emission envelope:

(1)   All waves with wave normal angles near the resonance cone angle result in ray paths which are _inside_ the limiting ray path and, hence, inside the outer envelope of the emission. The large field intensity near the envelope is the result of the very small spread in ray directions for wave normal directions near the resonance cone angle.

(2)   The frequency-time shape of the outer envelope can be understood in terms of the frequency dependence of the limiting

ray angle, ψ_{res}. Using the notation defined by Stix [1962], the limiting ray angle is given by

$$\tan^2 \psi_{res} = - S/P \quad . \tag{11}$$

If x is the horizontal distance (also proportional to the time coordinate on the spectrogram) from the symmetry axis of the emission and h is the altitude of the satellite above the source, then

$$(x/h)^2 = \tan^2 \psi_{res} = - S/P \quad . \tag{12}$$

The minimum frequency of the emission envelope (x = 0) can now be identified as the LHR frequency, where S = 0 [see Stix, 1962]. The shape of the emission envelope near the LHR frequency can be approximated by expanding S in a Taylor series about $f = f_{LHR}$ and neglecting higher order terms

$$S = \frac{\partial S}{\partial f} (f - f_{LHR}) \quad ,$$

which upon substituting into Eq. (12) becomes

$$(x/h)^2 = \frac{-\partial S/\partial f}{P} (f - f_{LHR}) \quad .$$

(13)

Equation (13) above shows that in the neighborhood of the LHR frequency, where $\partial S/\partial f$ and P can be regarded as constant, the emission envelope is a parabola.

At higher frequencies the shape of the emission envelope depends on the detailed plasma parameters. If the electron plasma frequency, f_p, is less than the electron gyrofrequency, f_g, then the envelope asymptotically approaches the electron plasma frequency as shown in Fig. 25, since P goes to zero at $f = f_p$. If f_p is greater than f_g, then the envelope asymptotically approaches the electron gyrofrequency, since S becomes infinite at $f = f_g$. Thus, the upper frequency limit is either f_p or f_g, whichever is smaller. Since the upper frequency limit of the Injun 5 wide-band receiver is well below either the electron gyrofrequency or plasma frequency, the flaring of the emission envelope at higher frequencies, as shown in Fig. 25(d), has not yet been experimentally verified.

In order to provide a rough quantitative verification of this explanation of the emission envelope shape, Eq. (12) was fit

to the envelope of the saucer shown in Fig. 22 using values of the gyrofrequency and plasma frequency computed at the satellite, even though this equation was derived under the rather unrealistic assumption of a completely homogeneous ionosphere with straight-line ray paths. The electron gyrofrequency at the satellite during this event was determined to be $f_g = 602$ kHz from the Jensen and Cain [1962] expansion for the geomagnetic field, and the electron plasma frequency was determined to be $f_p = 200$ kHz from the AFCRL electron density probe on Injun 5 [R. Sagalyn, personal communication]. For these rather low density conditions, with $f_p^2 \ll f_g^2$, S in Eq. (12) can to a very good approximation be written

$$S = 1 - \frac{f_{LHR}^2}{f^2} \, .$$

Since $P = 1 - f_p^2/f^2$ [Stix, 1962], Eq. (12) becomes

$$(x/h)^2 = \frac{f^2 - f_{LHR}^2}{f_p^2 - f^2} \, .$$

Using f_p = 200 kHz and f_{LHR} = 1.7 kHz (estimated from the minimum frequency of the emission envelope), (13) above was found to provide an excellent fit to the envelope of the saucer shown in Fig. 22 if the source was located at h = 1100 km below the satellite or at an altitude of about 1400 km. Since this source location assumed straight-line ray paths, it should be emphasized that this calculation gives a "virtual source location" which may differ somewhat from the actual source location when vertical gradients in the ionosphere are considered. Nevertheless, the excellent agreement between the observed shape of the emission envelope and Eq. (13) and the physically reasonable virtual source altitude predicted shows that this proposed explanation of the saucer envelope is quantitatively reasonable. For very narrow saucers, such as the examples in Fig. 24, the virtual source altitude would be much higher, nearer the satellite.

When vertical gradients in the ionosphere are considered, the detailed shape of the emission envelope must, in general, be determined by numerical integration. If the electron plasma frequency and the LHR frequency decrease monotonically with increasing altitude as shown in Fig. 26(a), then the limiting ray paths and the corresponding emission envelope will have the form illustrated in Figs. 26(b) and 26(c). The altitude dependence

of the plasma frequency causes the ray paths to diverge as illustrated in Fig. 26(b) because ψ_{res} increases with increasing altitude. This divergence has the effect of lowering the source altitude below the source altitude computing using Eq. (13).

The low-frequency cutoff at f_{LHR} (source) occurs because there is no limiting ray path ($\tan^2 \psi_{res}$ is negative) for altitudes where the wave frequency is less than the LHR frequency. The gap in the emission envelope at f_{LHR} (source) occurs because the two limiting ray paths at this frequency diverge as they propagate upward into the ionosphere. For frequencies below the LHR frequency, the ray paths are a sensitive function of the initial wave normal angle and no general statements can be made concerning propagation at these frequencies.

Effects due to this "gap" in the emission envelope are often clearly evident in the saucer-shaped emissions observed with Injun 5. Near the minimum frequency of the emission the envelope often becomes very indistinct and poorly defined, as can be seen for the saucer shown in Fig. 22. In some cases the emission almost completely disappears in the gap region as could be expected from the ray path model illustrated in Fig. 26. As might be expected, irregularities in the symmetry of the saucer envelope are not as common in the extremely narrow saucers such

as those illustrated in Fig. 24. If it is assumed that vertical
ionospheric gradients are responsible for such effects as the
gap at the minimum frequency of emission and horizontal gradients
are responsible for asymmetries in the envelope (with respect to
the horizontal distance, or time, axis), then one would expect
the effects of these gradients to be minimized for sources very
near the satellite. Thus, the very narrow saucers should be
expected to fit the simplified envelope of Fig. 25 more closely
than the saucers of much longer duration.

The propagation model described above accounts for most
of the general characteristics of the saucer-shaped emissions,
and is believed to be essentially correct. However, many detailed
questions remain to be investigated, including (1) the actual
source altitude, (2) the source geometry (point, line, sheet, or
extended source), (3) the emission mechanism and related particle
fluxes, and (4) the detailed origin of the proton cyclotron har-
monics sometimes observed.

NOTE: An explanation of the saucer-shaped emission similar
to that presented above has been advanced independently by R. L.
Smith [personal communication].

IV. SUMMARY

Several conclusive results have been obtained from the
Poynting flux measurements presented in the previous chapters.
The results for proton whistlers, subprotonospheric whistlers,
periodic emissions, and reflection phenomena mainly serve to
strengthen present theories or as an indicator of the validity
of the Poynting flux measurement. On the other hand, the follow-
ing new results have been obtained in the studies of ELF hiss,
VLF hiss, and saucer-shaped emissions:

(1)   A new propagation phenomenon has been observed in which
        downgoing ELF hiss, and possibly chorus, propagates across
        the plasmapause boundary and becomes subsequently reflected
        and trapped within the plasmasphere.

(2)   The observations of both downgoing and upgoing VLF hiss
        are consistent with an emission mechanism in which hiss
        is generated by Cerenkov, and possibly cyclotron, radiation
        and in which downgoing hiss is reflected below the altitude
        at which the wave frequency equals the LHR frequency. A
        new type of VLF hiss has been observed, called mid-latitude
        hiss, which occurs at sub-auroral-zone latitudes.

(3)   A new type of phenomenon called a saucer has been observed
       and qualitatively explained in terms of a frequency depen-
       dent limiting ray angle for propagation from a source at
       low altitudes below the satellite.

APPENDIX: INJUN 5 PHASE CALIBRATIONS

The accuracy of the Poynting flux measurements presented
in this thesis depends upon the preservation of the relative phase
between the wave electric and magnetic fields during the process
of receiving, transmitting, and demodulating the electric and
magnetic signals. Since frequency-dependent phase shifts occur
during this process, prelaunch calibrations were performed so
that these phase shifts could be corrected prior to making the
correlation measurements. The procedure for performing these
calibrations is illustrated in the block diagram of Fig. 27.
In the calibrations, an ac signal is applied to the electric
dipole antenna and simultaneously, through a loop equivalent
circuit, to the magnetic receiver input. The loop equivalent
circuit is used in place of the loop antenna because 60 Hz power
line interference makes it impossible to operate the loop antenna
and preamplifier in the laboratory. The effective RMS magnetic
field for the loop equivalent circuit is linearly proportional
to the RMS input voltage to the circuit and the frequency response
of the loop equivalent circuit matches the frequency response of
the actual loop antenna to within ± 0.5 dB. With the 400 MHz
satellite telemetry transmitter operating, the telemetry signal

is received and demodulated. The relative phase between the electric and magnetic outputs of the subcarrier demodulator can then be measured to determine the relative phase shift through the entire system. The results of the phase shift calibrations are presented in Figs. 28 and 29. Figure 28 shows the calibration for the low band (30 Hz to 650 Hz) and Fig. 29 shows the high band (300 Hz to 10 kHz) calibration. The same subcarrier demodulator used in the prelaunch calibrations is used for the actual data analysis, so that the only instrumentation which might differ in actual operation from the calibration system is the telemetry receiver and tape recorder. However, if the bandwidth of the telemetry receiver is sufficiently wide so that the receiver has a flat response over the telemetry signal bandwidth, then there will be negligible phase shifts within the receiver. This requirement is satisfied for the data presented in this thesis.

A more serious problem arises when the telemetry receiver output is recorded on magnetic tape prior to being demodulated for the correlation measurement. The Injun 5 telemetry system transmits the high-band electric receiver data on a single-sideband subcarrier. When this single-sideband subcarrier is recorded on magnetic tape at the data acquisition station, the tape recording systems introduce a time-dependent and unpredictable

phase shift into the data which cannot be accurately calibrated.
This problem can be solved by decoding the telemetry data before
recording it on tape. In practice, the demodulator is installed
at the telemetry station and, after demodulation, the high-band
electric and magnetic data channels are recorded on two FM sub-
carrier frequencies on a single tape-recorder channel. This
system introduces only a small relative phase shift ($< 10°$)
which can be accurately calibrated. With this system, however,
only high-band data from a single telemetry station can be used
at a given time, since the demodulator must be installed at the
station. Due to the method by which the low-band data is
modulated for telemetry transmission (FM subcarrier modulation),
the above problem does not arise and the low-band data can be
recorded on magnetic tape prior to demodulation.

In performing the actual correlation measurements, all
phase shift corrections are applied with phase-shift networks
before processing the signals with the instrumentation of Fig. 3.
These corrections include those required by the prelaunch cali-
brations illustrated in Figs. 28 and 29, as well as the correc-
tion required by the FM subcarrier modulation of the high-band
data at the telemetry station. As discussed in Chapter I,
additional phase shifts are also introduced to ascertain that

errors of the order of ± 5 degrees in the prelaunch calibrations do not affect the Poynting flux determination.

REFERENCES

Burtis, W. J., and R. A. Helliwell, "Banded chorus--a new type of VLF radiation observed in the magnetosphere by OGO 1 and OGO 3," J. Geophys. Res., 74, 3002, 1969.

Carpenter, D. L., "Whistler studies of the plasmapause in the magnetosphere. 1. Temporal variations in the position of the knee and some evidence on plasma motions near the knee," J. Geophys. Res., 71, 693, 1966.

Carpenter, D. L., N. Dunckel, and J. F. Walkup, "A new very low frequency phenomenon: whistlers trapped below the protonosphere," J. Geophys. Res., 69, 5009, 1964.

Carpenter, D. L., F. Walter, R. E. Barrington, and D. J. McEwen, "Alouette 1 and 2 observations of abrupt changes in whistler rate and of VLF noise variations at the plasmapause--a satellite-ground study," J. Geophys. Res., 73, 2929, 1968.

Colin, Lawrence, and Stuart W. Dufour, "Charged particle temperatures and concentrations in the earth's exosphere," J. Geophys. Res., 73, 2967, 1968.

Gurnett, Donald A., "A satellite study of VLF hiss," J. Geophys. Res., 71, 5599, 1966.

Gurnett, Donald A., "Satellite observations of VLF emissions and their association with energetic particles," in Earth's Particles and Fields, ed. B. M. McCormac, Reinhold Book Corporation, New York, 1968.

Gurnett, D. A., S. D. Shawhan, N. M. Brice, and R. L. Smith, "Ion cyclotron whistlers," J. Geophys. Res., 70, 1665, 1965.

Gurnett, Donald A., and Thomas B. Burns, "The low-frequency cutoff of ELF emissions," J. Geophys. Res., 73, 7437, 1968.

Gurnett, Donald A., G. William Pfeiffer, Roger R. Anderson, Stephen R. Mosier, and David P. Cauffman, "Initial observations of VLF electric and magnetic fields with the Injun 5 satellite," J. Geophys. Res., 74, 4631, 1969.

Helliwell, R. A., Whistlers and Related Ionospheric Phenomena, Stanford University Press, Stanford, Calif., 1965.

Heyborne, R. L., R. L. Smith, and R. A. Helliwell, "Latitudinal cutoff of VLF signals in the ionosphere," J. Geophys. Res., 74, 2393, 1969.

Jensen, D. C., and J. C. Cain, "An interim geomagnetic field" (abstract), J. Geophys. Res., 67, 3568, 1962.

Jørgensen, T. Stockflet, "Interpretation of auroral hiss measured on OGO 2 and at Byrd Station in terms of incoherent Cerenkov radiation," J. Geophys. Res., 73, 1055, 1968.

Kennel, C. F., and H. E. Petschek, "Limit on stably trapped particle fluxes," J. Geophys. Res., 71, 1, 1966.

Liemohn, Harold B., "Radiation from electrons in magnetoplasma," Radio Science, 69D, 741, 1965.

Mansfield, V. N., "Radiation from a particle spiraling in a cold magnetoplasma," Astrophys. J., 147, 672, 1967.

McIlwain, C. E., "Coordinates for mapping the distribution of magnetically trapped particles," J. Geophys. Res., 66, 3681, 1961.

Mosier, Stephen R., and Donald A. Gurnett, "VLF measurements of the Poynting flux along the geomagnetic field with the Injun 5 satellite," J. Geophys. Res., 74, 5675, 1969.

Russell, Christofer T., Robert E. Holzer, and Edward J. Smith, "OGO 3 observations of ELF noise in the magnetosphere. 1. Spatial extent and frequency of occurrence," J. Geophys. Res., 74, 755, 1969.

Smith, R. L., "Guiding of whistlers in a homogeneous medium," J. Res. Natl. Bur. Std., 64D, 505, 1960.

Smith, R. L., "An explanation of subprotonospheric whistlers," J. Geophys. Res., 69, 5019, 1964.

Stix, T. H., The Theory of Plasma Waves, McGraw-Hill Book Company, New York, 1962.

Storey, L. R. O., "An investigation of whistling atmospherics," Phil. Trans. Roy. Soc. London [A], 246, 113, 1953.

Storey, L. R. O., and J. C. Cerisier, "An interpretation of the noise bands observed near the lower hybrid resonance frequency by artificial satellites," Compt. Rend., t. 266, 525, 1968.

Swift, D. W., "A new interpretation of VLF chorus," J. Geophys. Res., 73, 7447, 1968.

Thorne, R. M., and C. F. Kennel, "Quasi-trapped VLF propagation in the outer magnetosphere," J. Geophys. Res., 72, 857, 1967.

Figure 1.   Top view of the Injun 5 satellite showing the orien-
tation of the electric dipole and magnetic loop
antenna.
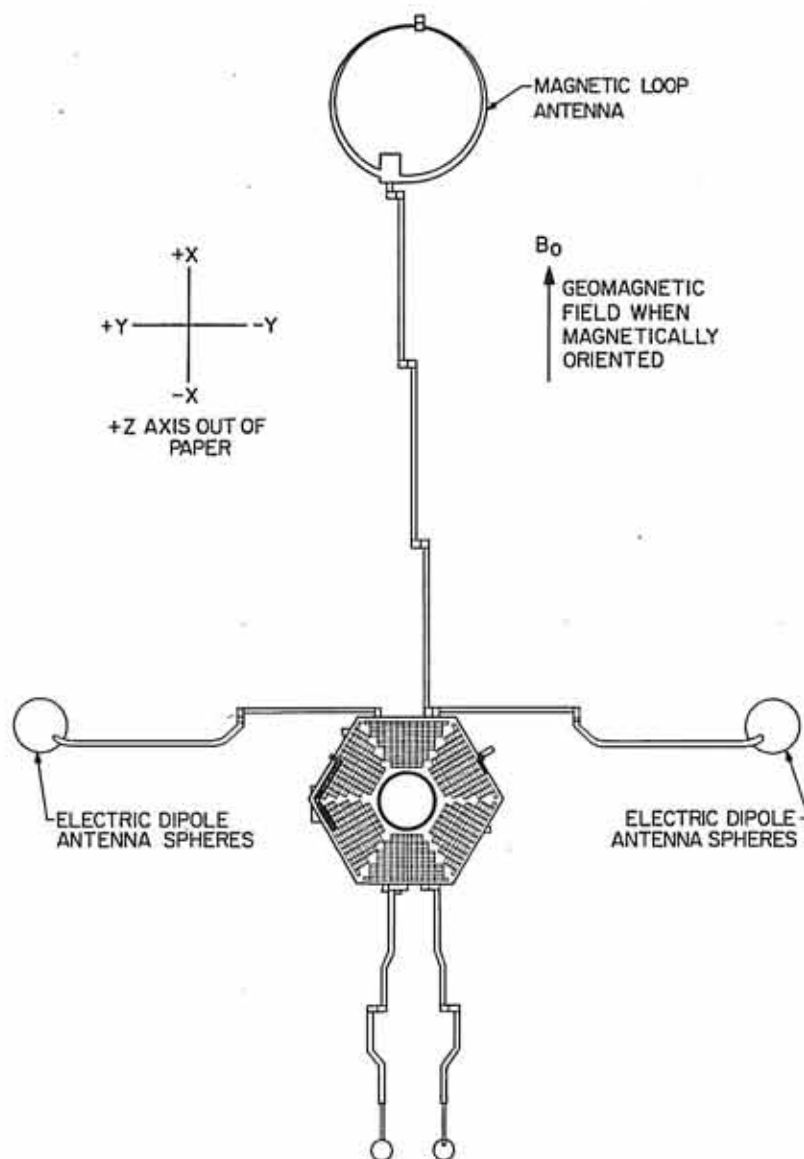
TOP VIEW
OF INJUN $\underline{V}$

FIGURE 1

Figure 2.   Orientation geometry for the Injun 5 satellite showing

azimuthal rotation ψ and antenna misalignment angles

δ_E and δ_B.

A-G69-692

GEOMAGNETIC
FIELD

SATELLITE MISALIGNMENT
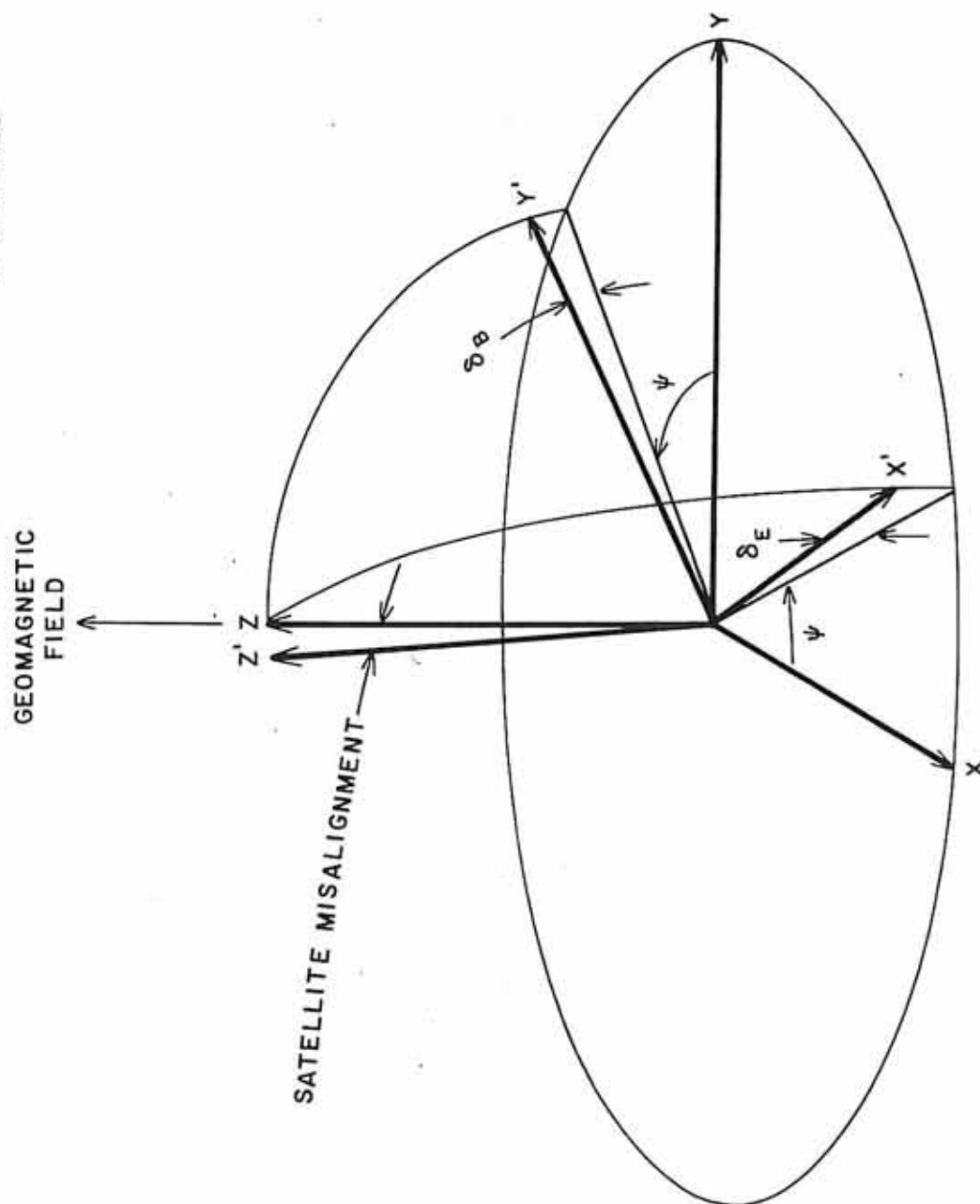
FIGURE 2

Figure 3.   Block diagram of the instrumentation used to determine the direction of the Poynting flux along the geomagnetic field.

B-G69-178
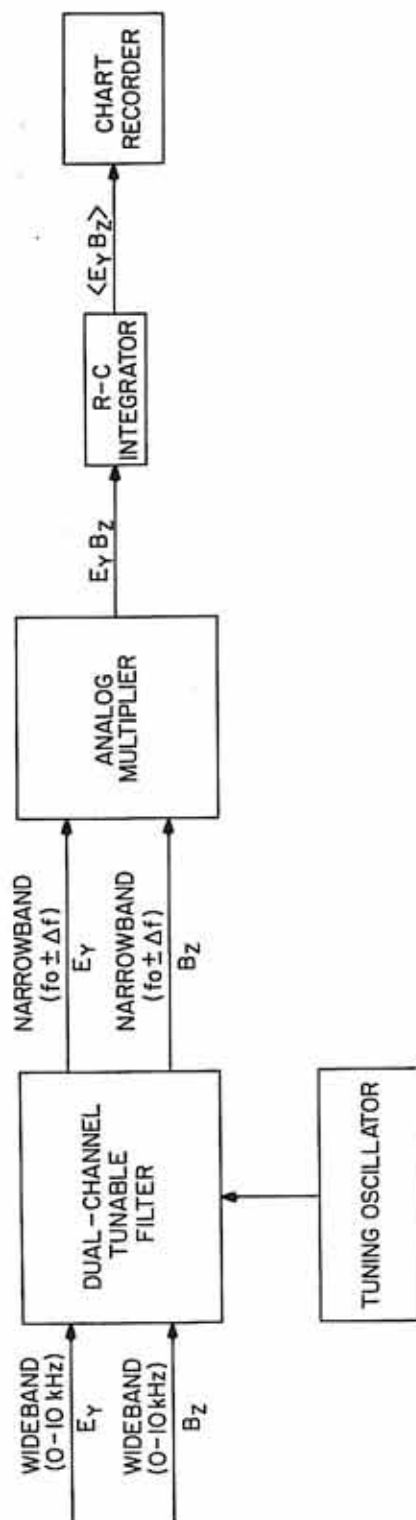
FIGURE 3

Figure 4.   Correlation measurement of a group of proton whistlers.
Proton whistlers are propagating up the geomagnetic
field lines, in agreement with theory.
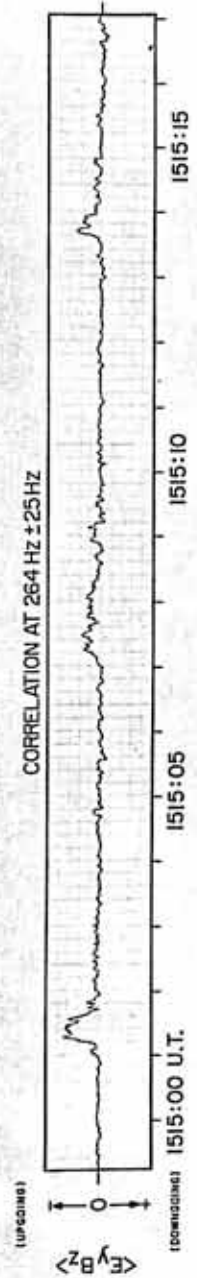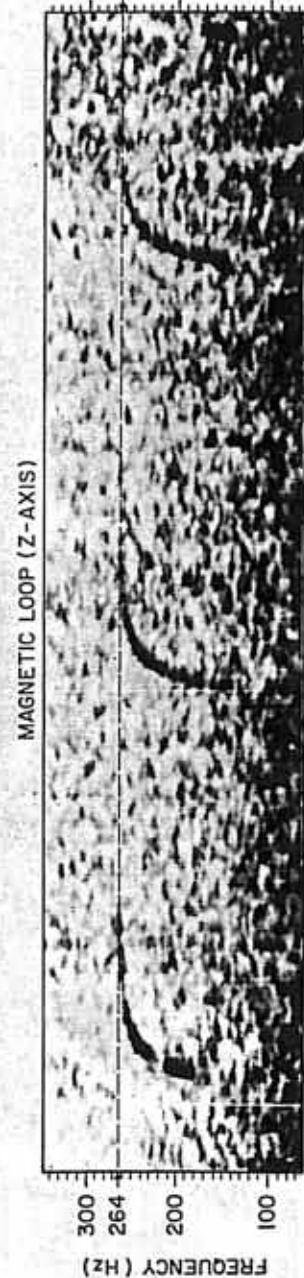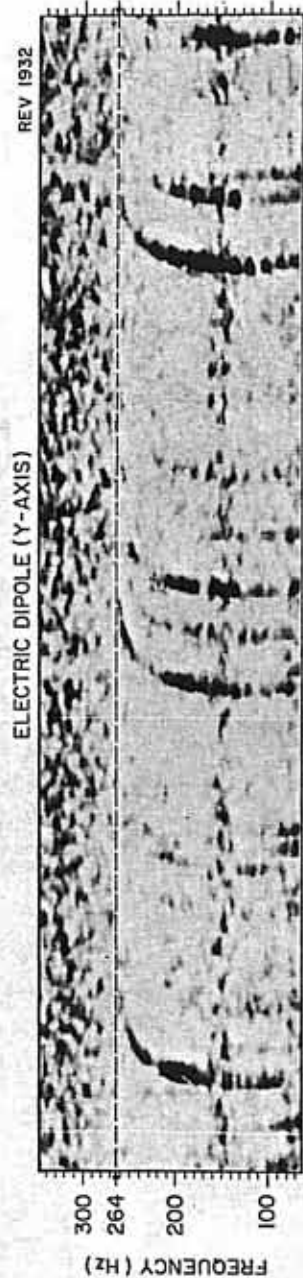
FIGURE 4

Figure 5.   Correlation measurement of discrete VLF emissions,
             indicating that downgoing waves are being reflected
             in the lower ionosphere and are propagating back to
             the satellite.

INVARIANT LATITUDE   56.6°
ALTITUDE   1336 KM
MAGNETIC LOCAL TIME   18.36 HR

D-G69-425-2

MAGNETIC LOOP (Z-AXIS)   REV 1937

IMPEDANCE MEASUREMENT

ELECTRIC DIPOLE (Y-AXIS)

CORRELATION AT 1300 Hz ± 25 Hz

$\langle E_y B_z \rangle$

(UPGOING)
0
(DOWNGOING)

0140:15 U.T.   0140:20   0140:25

JANUARY 15, 1969
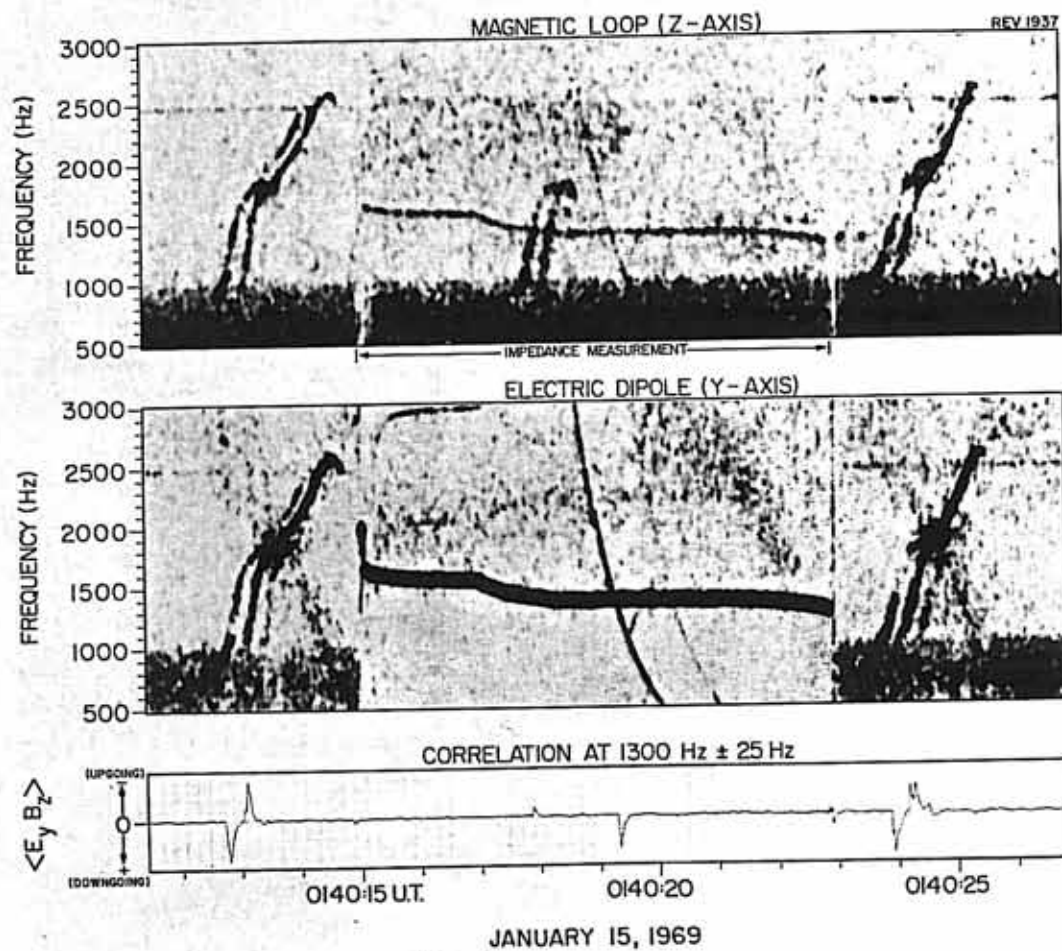
FIGURE 5

Figure 6. Correlation measurement of subprotonospheric whistlers,
showing multiple reflections between the lower iono-
sphere and a region near the base of the protonosphere.

B-G69-758-2

INVARIANT LATITUDE   44.3°
ALTITUDE   723 KM
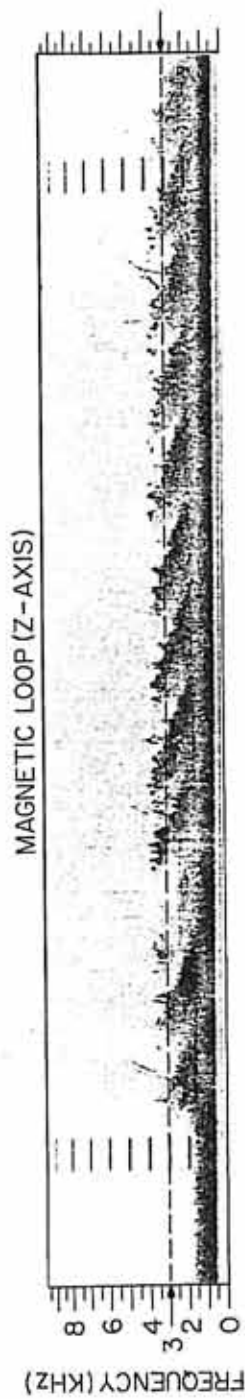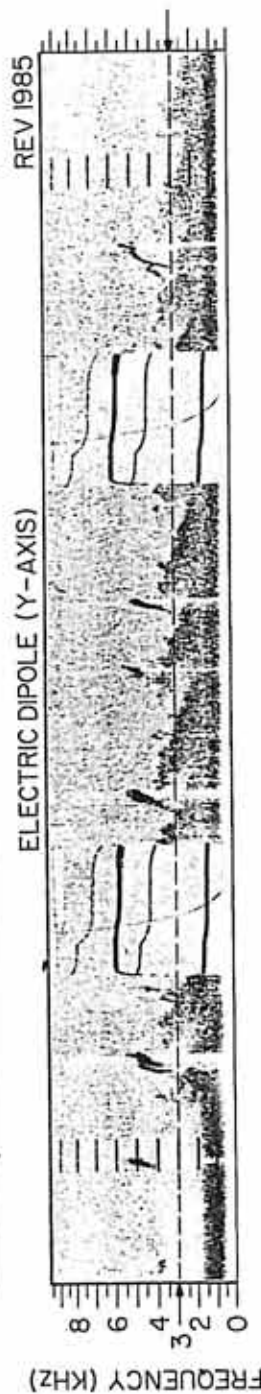MAGNETIC LOCAL TIME   21.04 HR
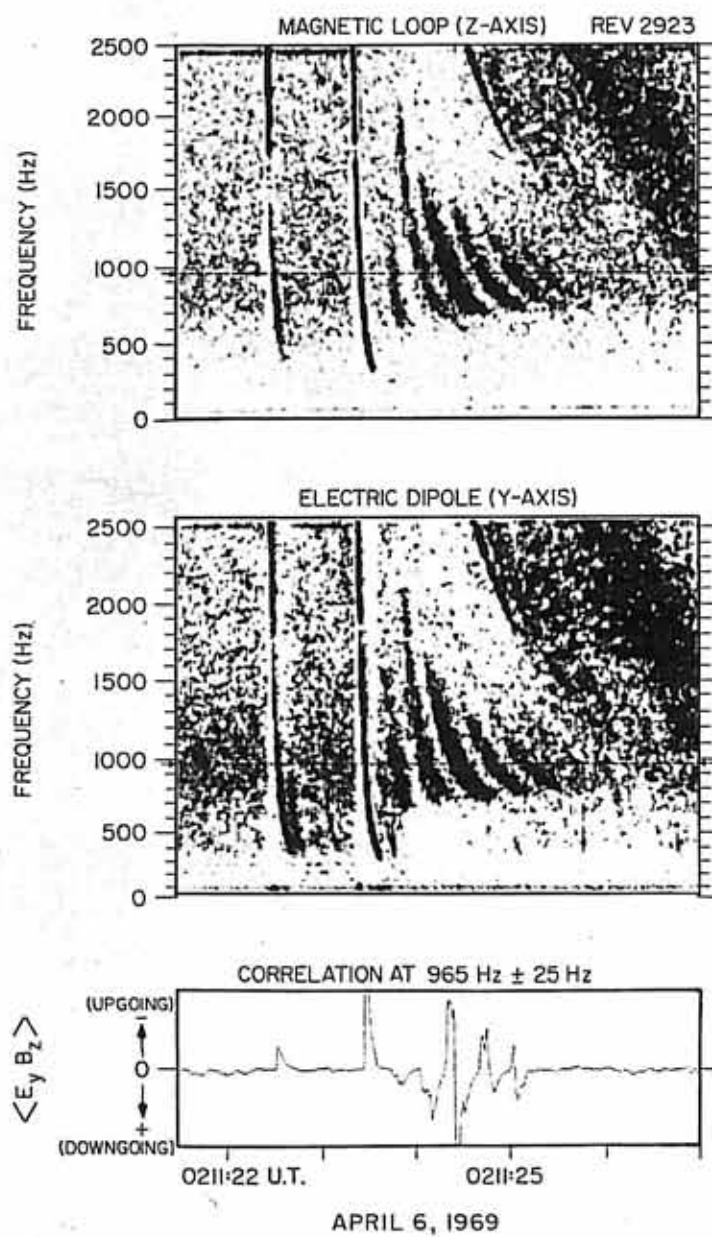
FIGURE 6

Figure 7.   Correlation measurement of non-dispersive periodic

emission.   The observed emission is believed to have

"leaked" from the field line on which the echoing is

taking place.

C-G69-209-4

58.1° INVARIANT LATITUDE
1209 KM ALTITUDE
18.14 HR MAGNETIC LOCAL TIME

60.9°
1256 KM
18.16 HR

REV 1985

ELECTRIC DIPOLE (Y-AXIS)

MAGNETIC LOOP (Z-AXIS)

FREQUENCY (kHz)

FREQUENCY (kHz)

CORRELATION AT 3000 Hz ± 25 Hz

⟨E_y B_z⟩

(UPGOING) (DOWNGOING)

0021:00 U.T. 0021:30 0022:00

JANUARY 19, 1969
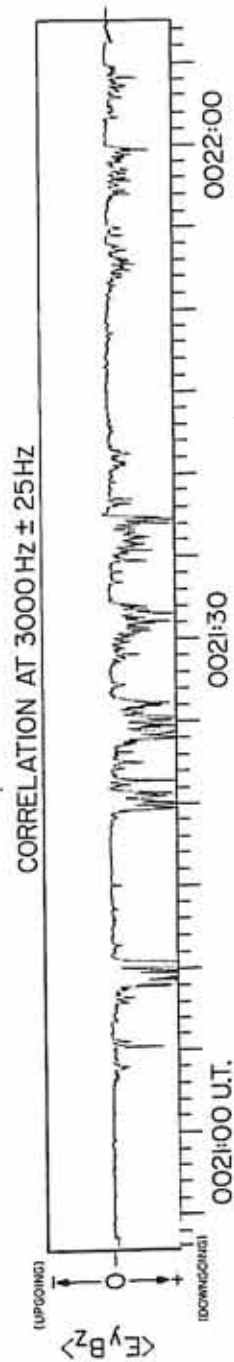
FIGURE 7

Figure 8.   Correlation measurement of dispersive periodic emission.
The observed emission is believed to have "leaked" from
the field line on which the echoing is taking place.

FIGURE 8

FEBRUARY 4, 1969
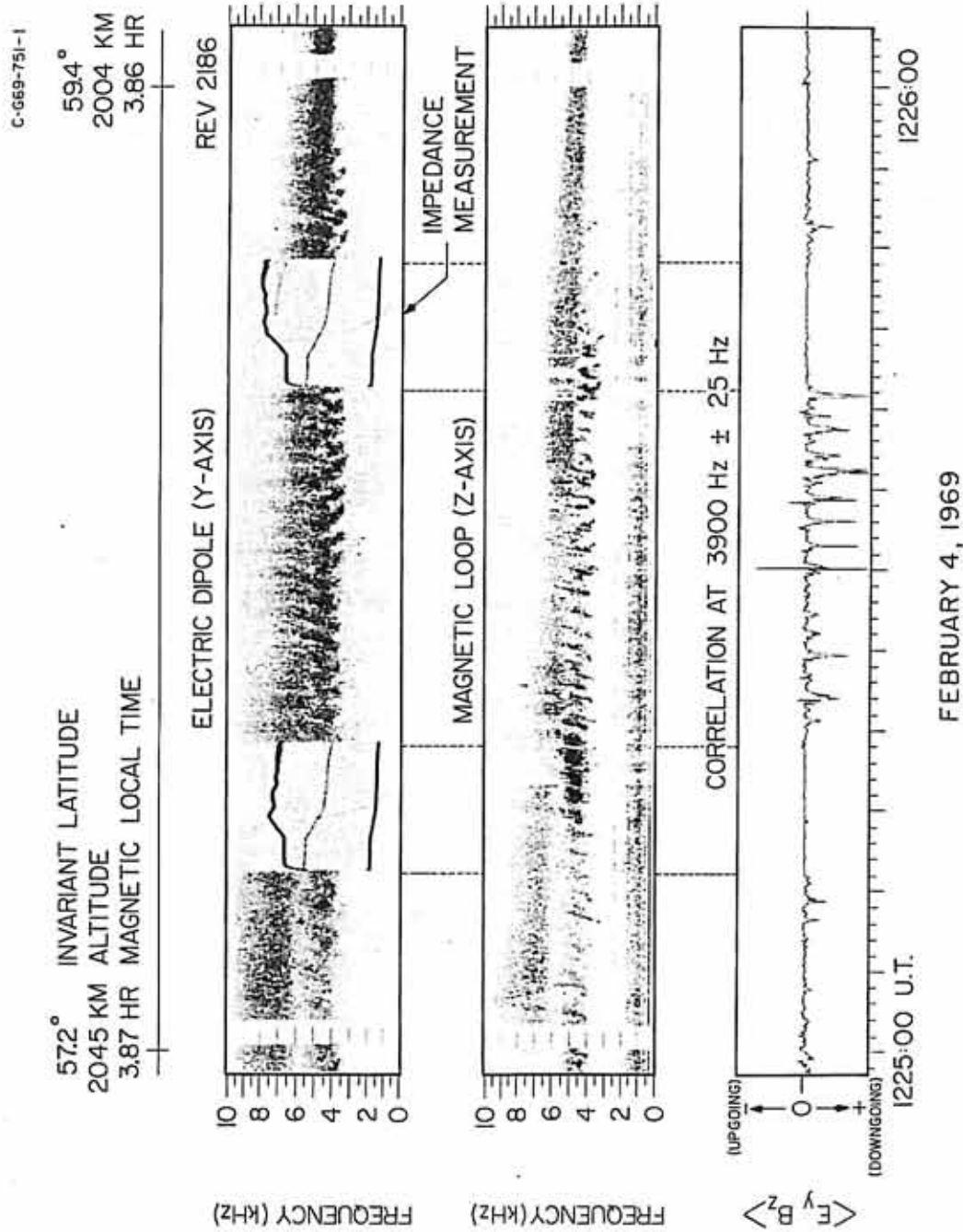
Figure 9.   Correlation measurement of ELF hiss. At frequencies

above the low-frequency cutoff, only downgoing waves

are observed whereas at the cutoff frequency, both

upgoing and downgoing waves are observed, suggesting
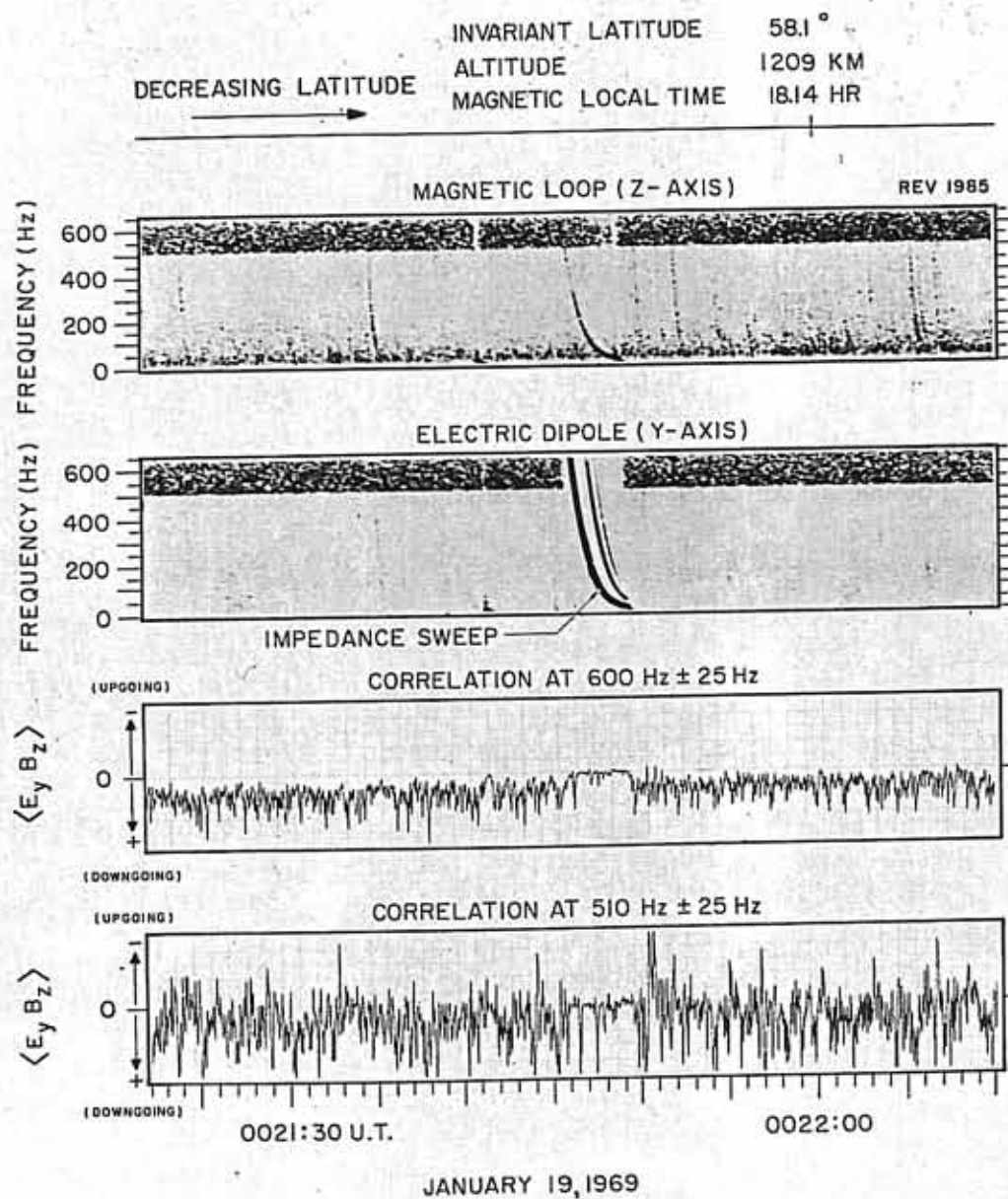
that the waves are being reflected.

C-G69-375-1

INVARIANT LATITUDE 58.1°
ALTITUDE 1209 KM
MAGNETIC LOCAL TIME 18.14 HR

DECREASING LATITUDE →

MAGNETIC LOOP (Z-AXIS) REV 1985

ELECTRIC DIPOLE (Y-AXIS)

IMPEDANCE SWEEP

(UPGOING) CORRELATION AT 600 Hz ± 25 Hz

(DOWNGOING)

(UPGOING) CORRELATION AT 510 Hz ± 25 Hz

(DOWNGOING) 0021:30 U.T. 0022:00

JANUARY 19, 1969

FIGURE 9

Figure 10.   Correlation measurement of ELF hiss for a plasmapause

crossing in which a transition from upgoing to down-

going waves occurred.   The electron density from the

AFCRL probe is also plotted and indicates that the

transition occurs at the "knee" in the electron

density gradient.
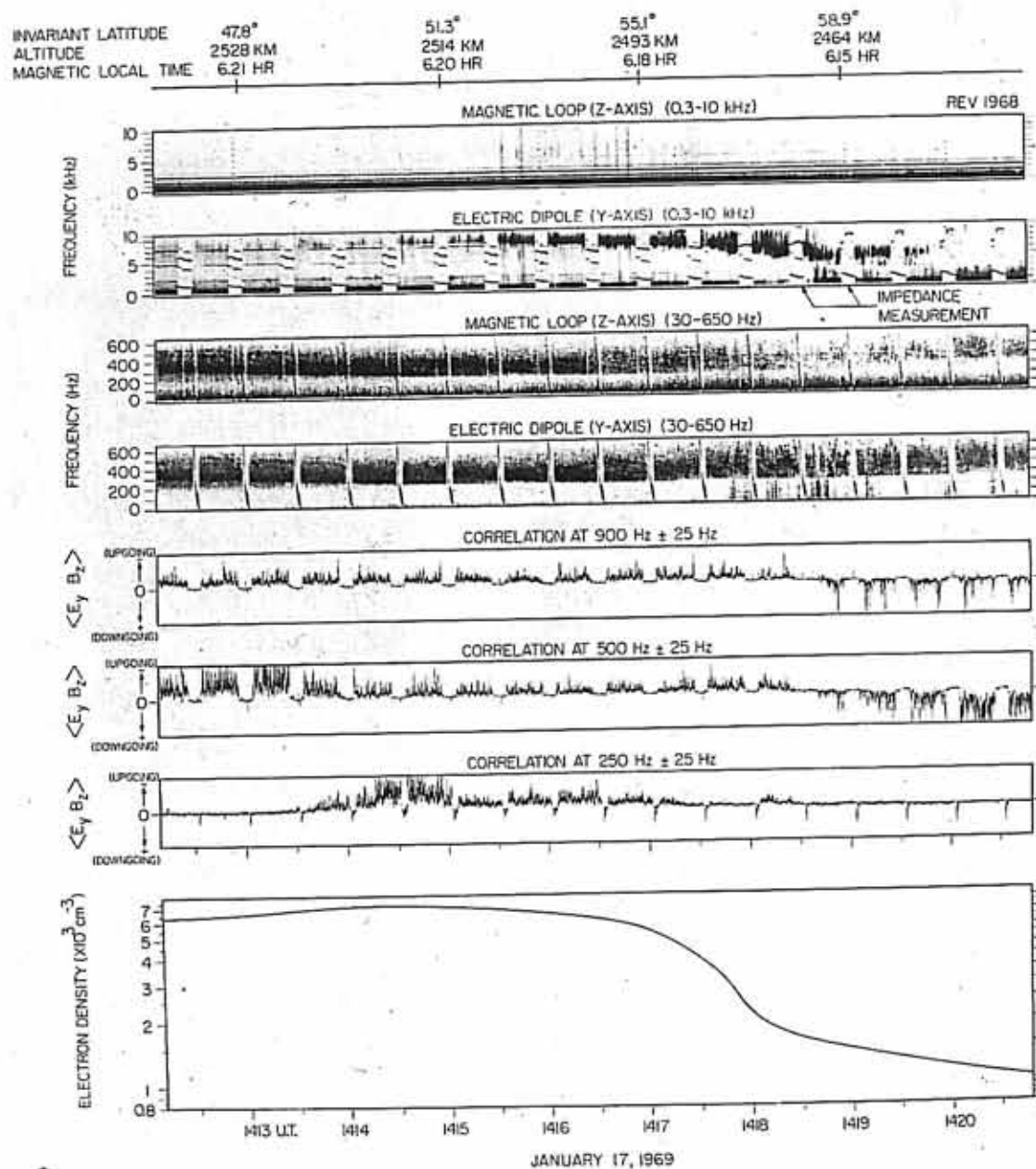
FIGURE 10

Figure 11.   Injun 5 orbit plots for times during which downgoing ELF hiss was observed.

A-G69-661
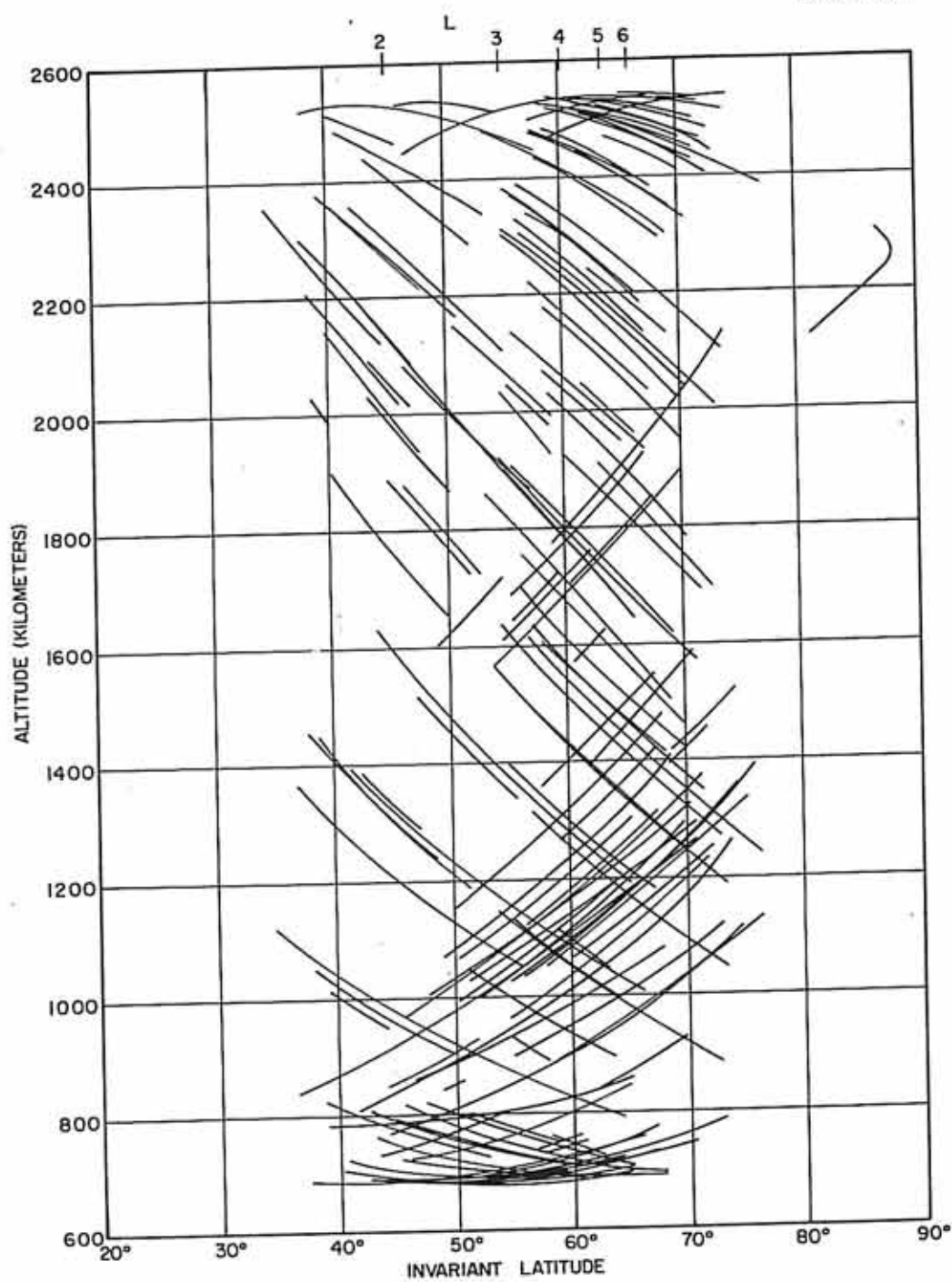
FIGURE 11

Figure 12.   Injun 5 orbit plots for times during which upgoing
              ELF hiss was observed. No upgoing hiss was observed
              at altitudes greater than approximately 60° INVL.
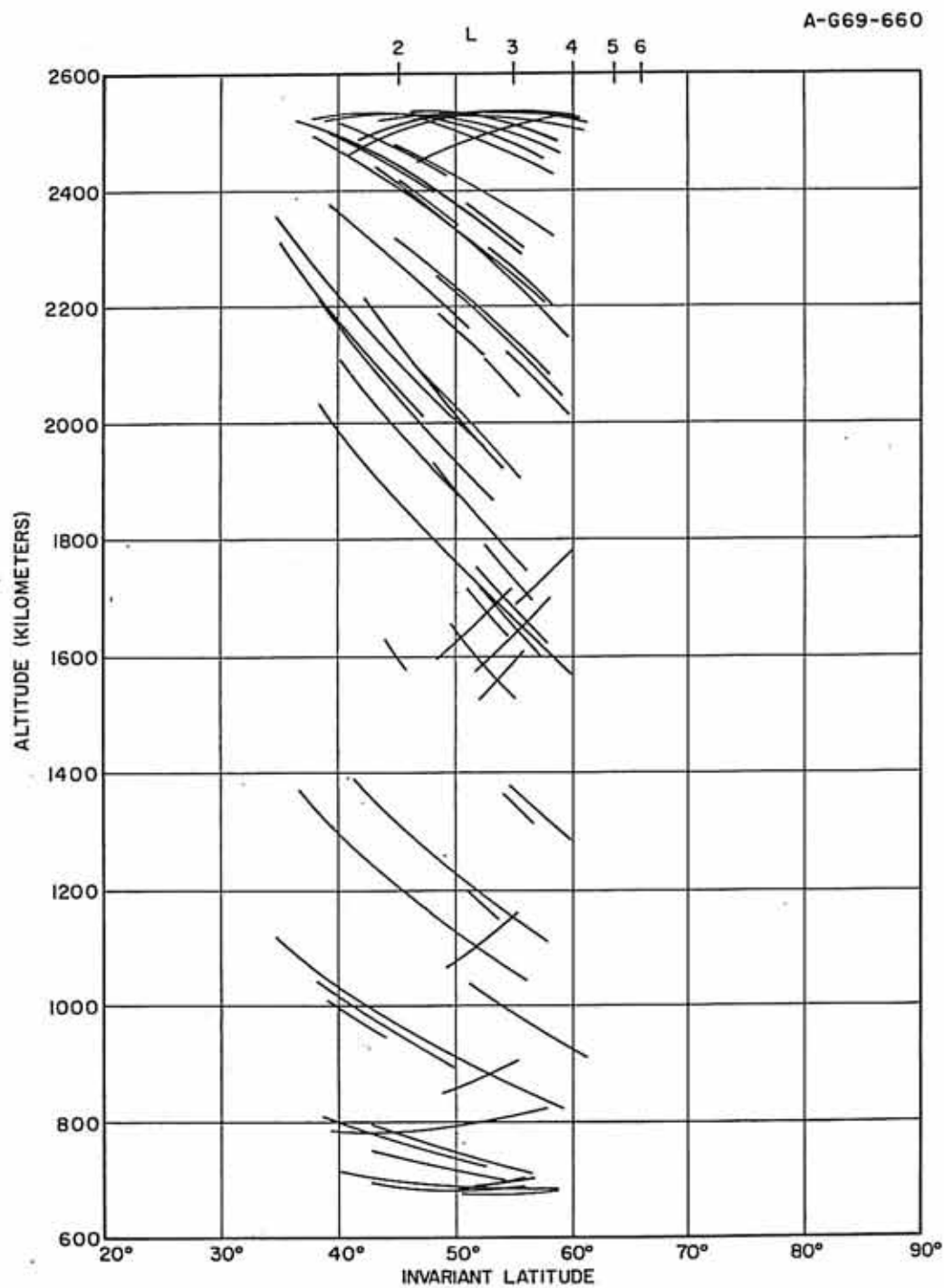
FIGURE 12

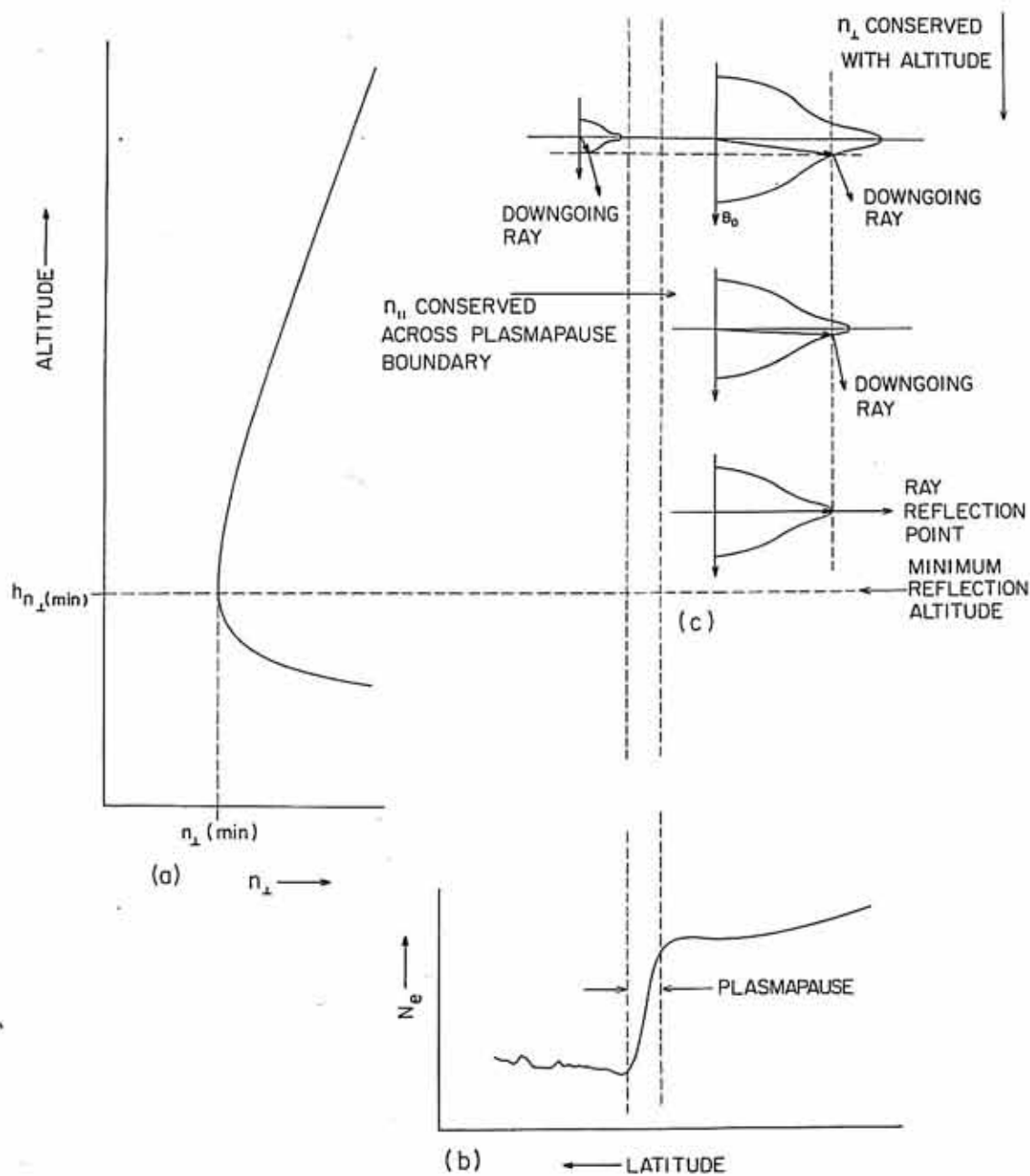Figure 13. Diagram showing reflection mechanism of ELF hiss in the plasmasphere.

FIGURE 13

Figure 14.   Correlation measurement of downgoing VLF chorus

observed at 69.9° INVL.

C-G69-1B3-3

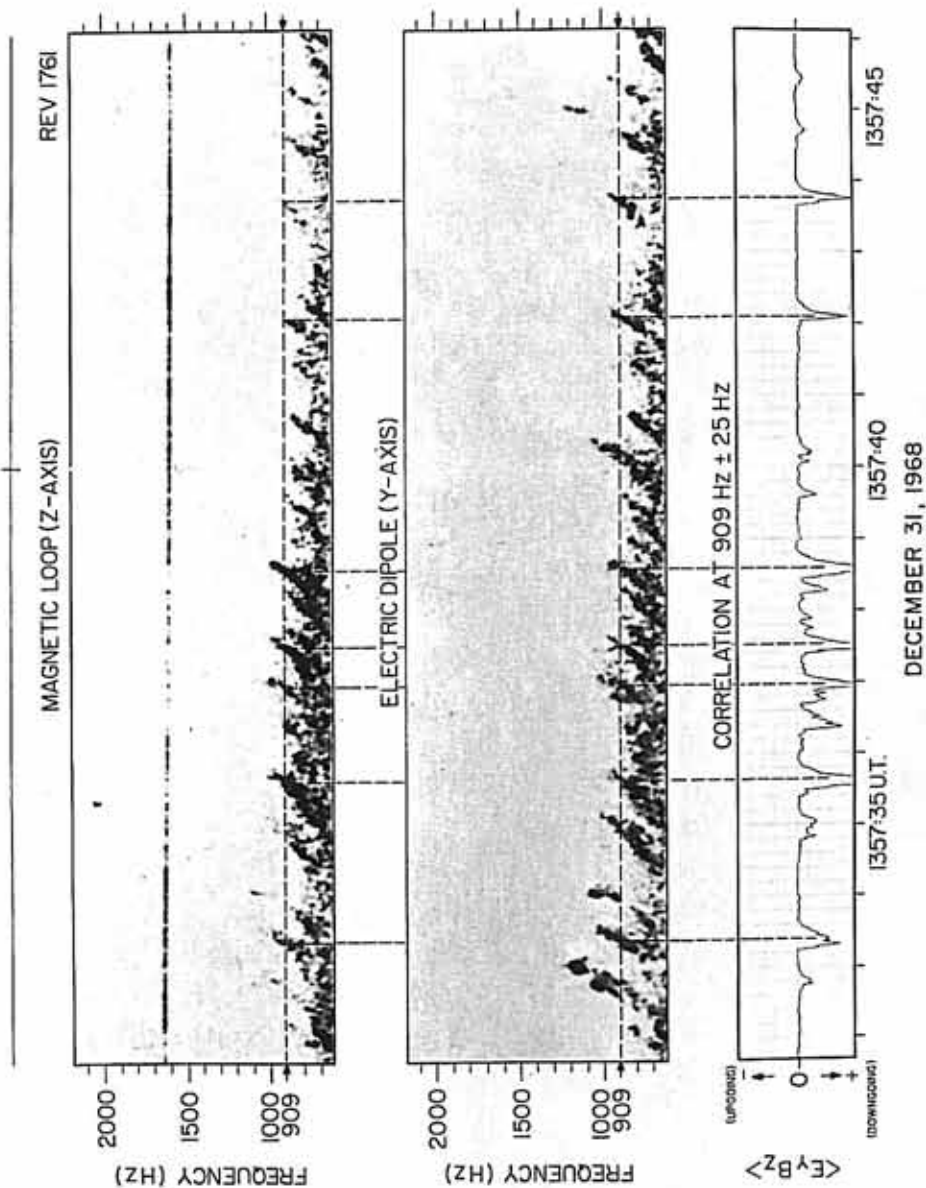INVARIANT LATITUDE 69.9°
ALTITUDE 2530 KM
MAGNETIC LOCAL TIME 8.74 HR

MAGNETIC LOOP (Z-AXIS)

ELECTRIC DIPOLE (Y-AXIS)

CORRELATION AT 909 Hz ± 25 Hz

REV 1761

1357:45   1357:40   1357:35 U.T.

DECEMBER 31, 1968

FIGURE 14

Figure 15.   Correlation measurement of upgoing VLF chorus

observed at 51.4° INVL.

INVARIANT LATITUDE 51.4°
ALTITUDE 2530 KM
MAGNETIC LOCAL TIME 6.26 HR

REV 1966

ELECTRIC DIPOLE (Y-AXIS)

MAGNETIC LOOP (Z-AXIS)

CORRELATION AT 2600 HZ ± 25 HZ

1015:40 U.T.   1015:45   1015:50

JANUARY 17, 1969
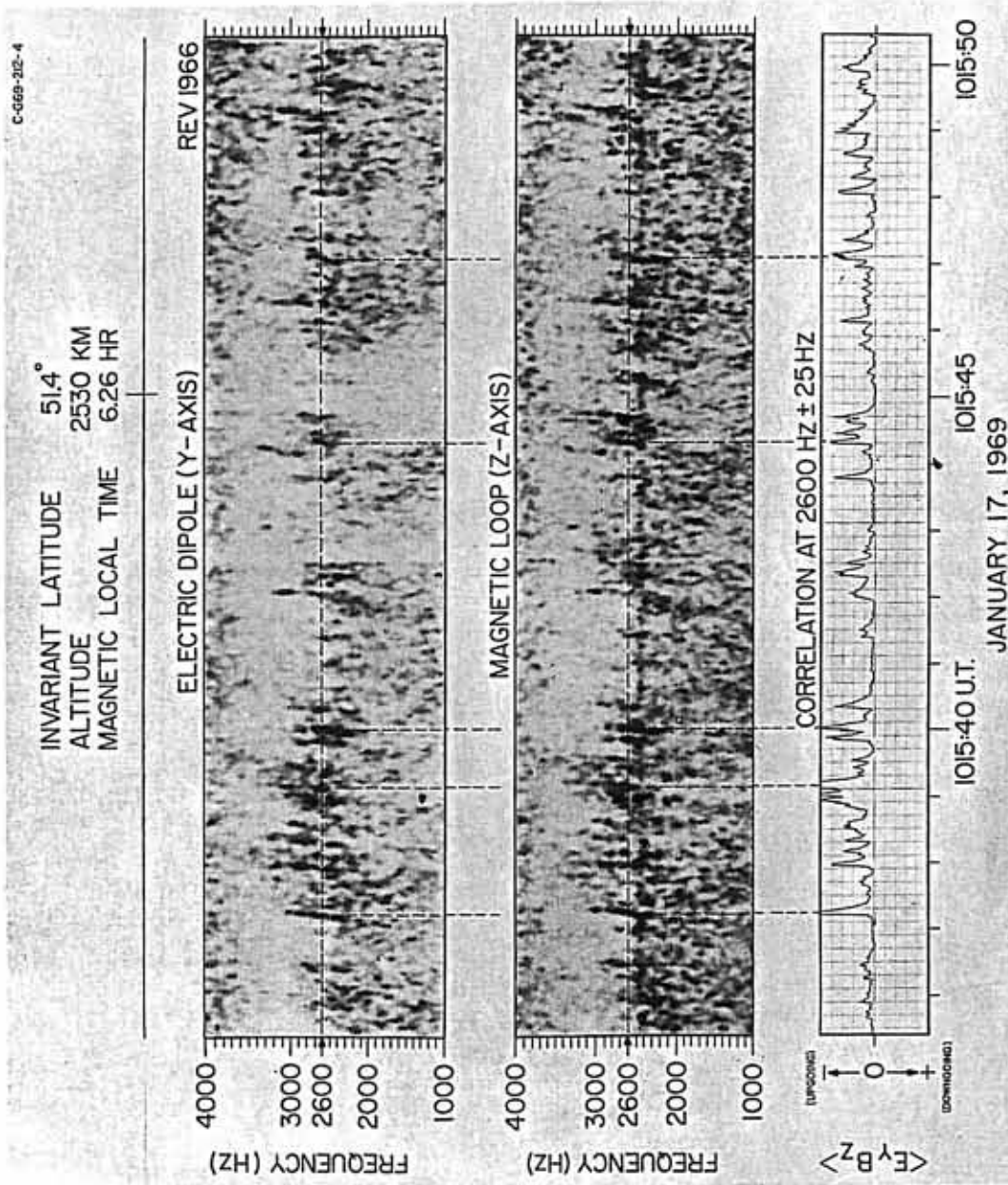
FIGURE 15

Figure 16. Correlation measurement of impulsive auroral-zone VLF hiss, showing both downgoing and upgoing waves. The downgoing waves are much more intense than the upgoing waves.

C-669-713-I

65.4°
1126 KM
16.22 HR

REV 2056

68.4° INVARIANT LATITUDE
1172 KM ALTITUDE
16.10 HR MAGNETIC LOCAL TIME

MAGNETIC LOOP (Z-AXIS)

IMPEDANCE MEASUREMENT

ELECTRIC DIPOLE (Y-AXIS)

CORRELATION AT 7000 Hz ± 25 Hz

FREQUENCY (kHz)   FREQUENCY (kHz)

$\langle E_y \, B_z \rangle$

(UPGOING)   0   (DOWNGOING)

2023:00 U.T.   2023:30   2024:00

JANUARY 24, 1969
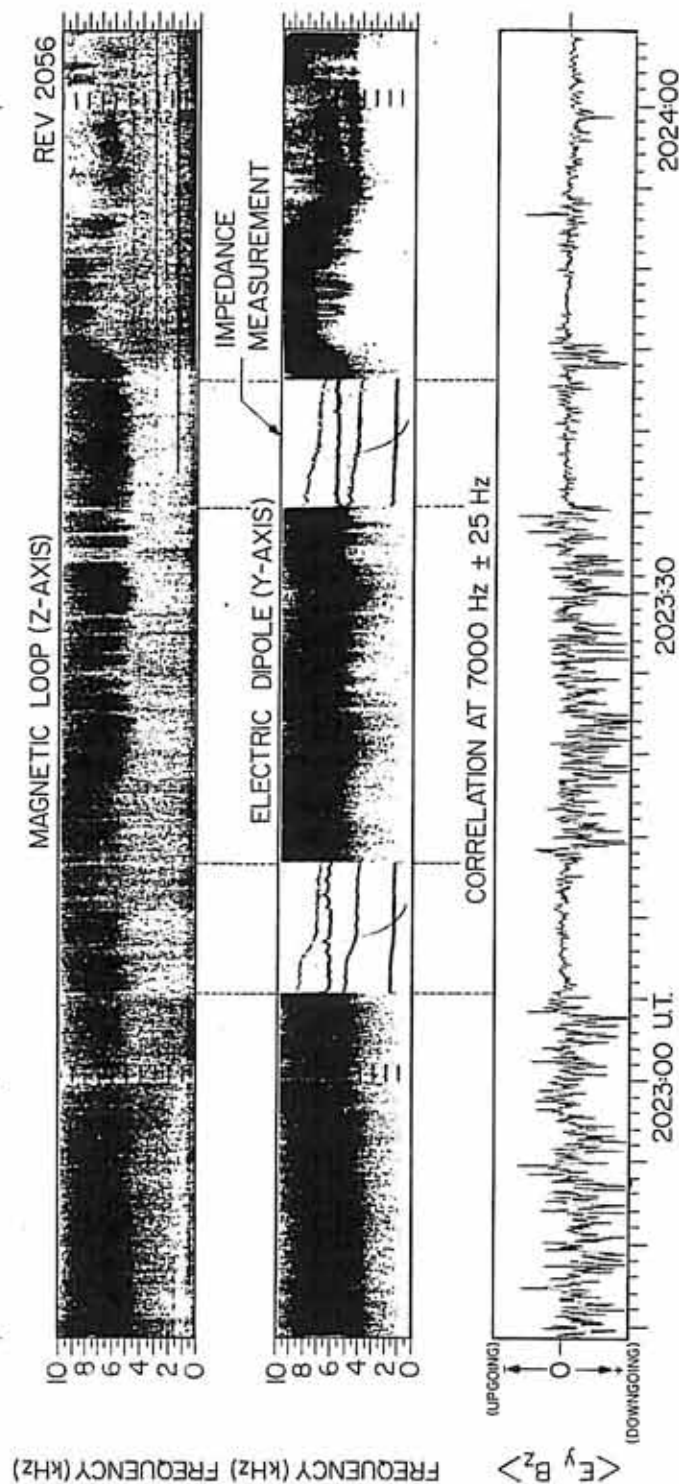
FIGURE 16

Figure 17.   Correlation measurement of auroral-zone VLF hiss

showing strong latitudinal dependence of lower

cutoff frequency.
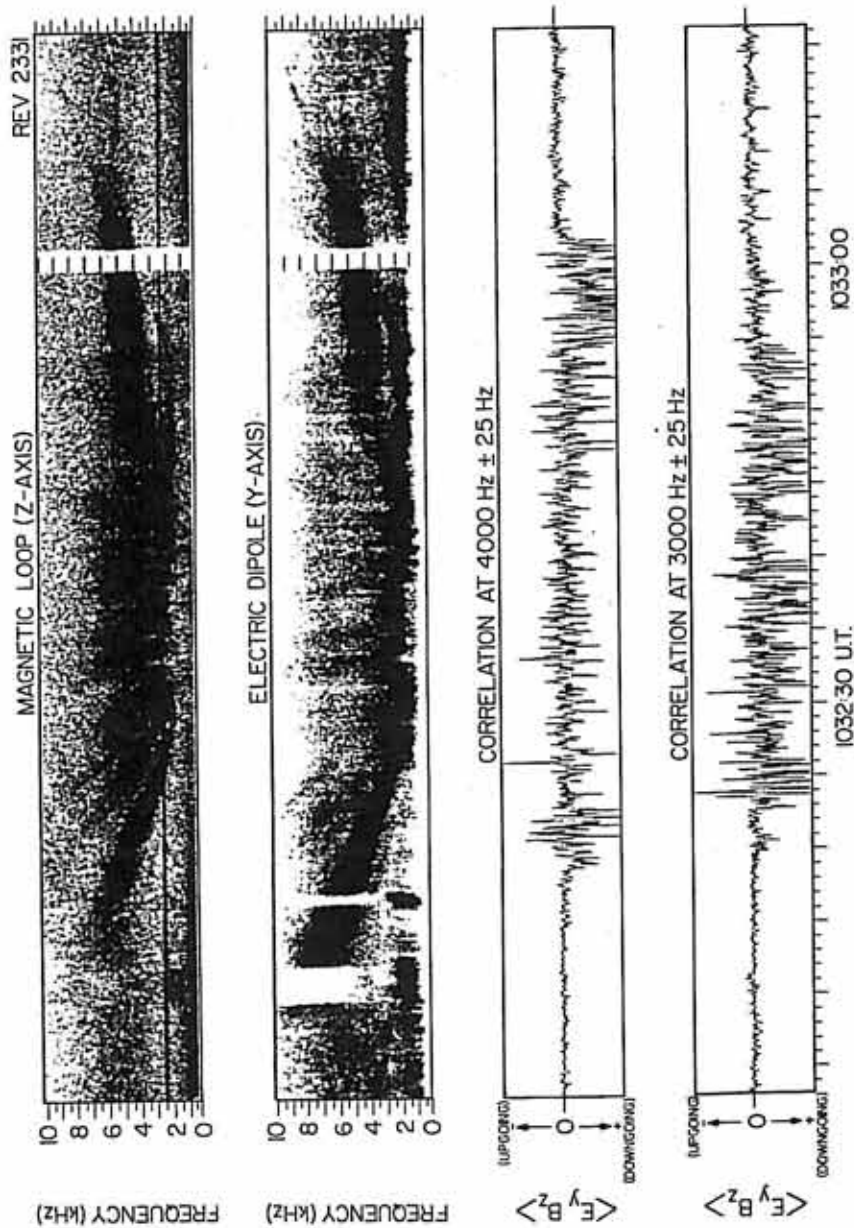
FIGURE 17

Figure 18.   Correlation measurement of a symmetric V-shaped VLF
              hiss event showing both downgoing and upgoing waves.

C-G69-691-2

6.94° INVARIANT LATITUDE
1445KM ALTITUDE
2.55HR MAGNETIC LOCAL TIME

REV 2331

MAGNETIC LOOP (Z-AXIS)

ELECTRIC DIPOLE (Y-AXIS)

CORRELATION AT 4000 Hz ± 25 Hz

CORRELATION AT 3000 Hz ± 25 Hz

FREQUENCY (kHz)

FREQUENCY (kHz)

$\langle E_y B_z \rangle$
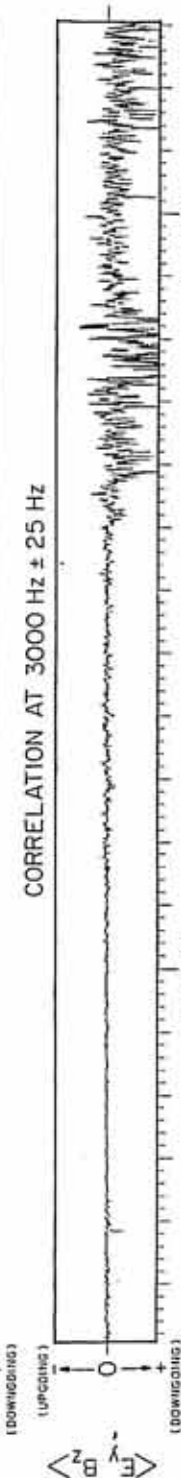
$\langle E_y B_z \rangle$

1032:30 U.T.

1033:00

FEBRUARY 16, 1969

FIGURE 18

Figure 19.   Correlation measurement of a V-shaped VLF hiss event
consisting of segments of narrow emission bands,
showing both downgoing and upgoing waves.

ELECTRIC DIPOLE (Y-AXIS)

MAGNETIC LOOP (Z-AXIS)

CORRELATION AT 6000 Hz ± 25 Hz

CORRELATION AT 3000 Hz ± 25 Hz

REV 1778

INVARIANT LATITUDE   78.5°   78.6°
ALTITUDE   2071 KM   2029 KM
MAGNETIC LOCAL TIME 17.10 HR   17.49 HR

2353:00   2354:00

JANUARY 1, 1969

FIGURE 19

C-G69-750-1

Figure 20.   Correlation of sharply-banded VLF hiss resembling
              V-shaped hiss. The wave magnetic field is too weak
              to be seen in the magnetic receiver spectrogram.
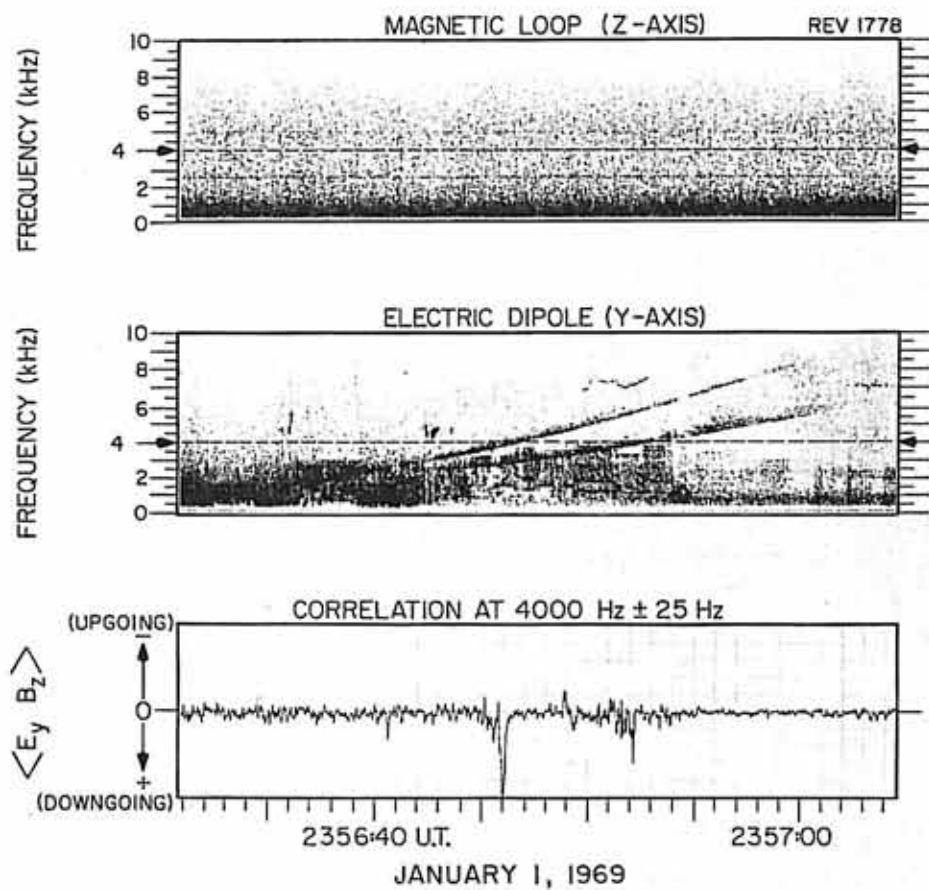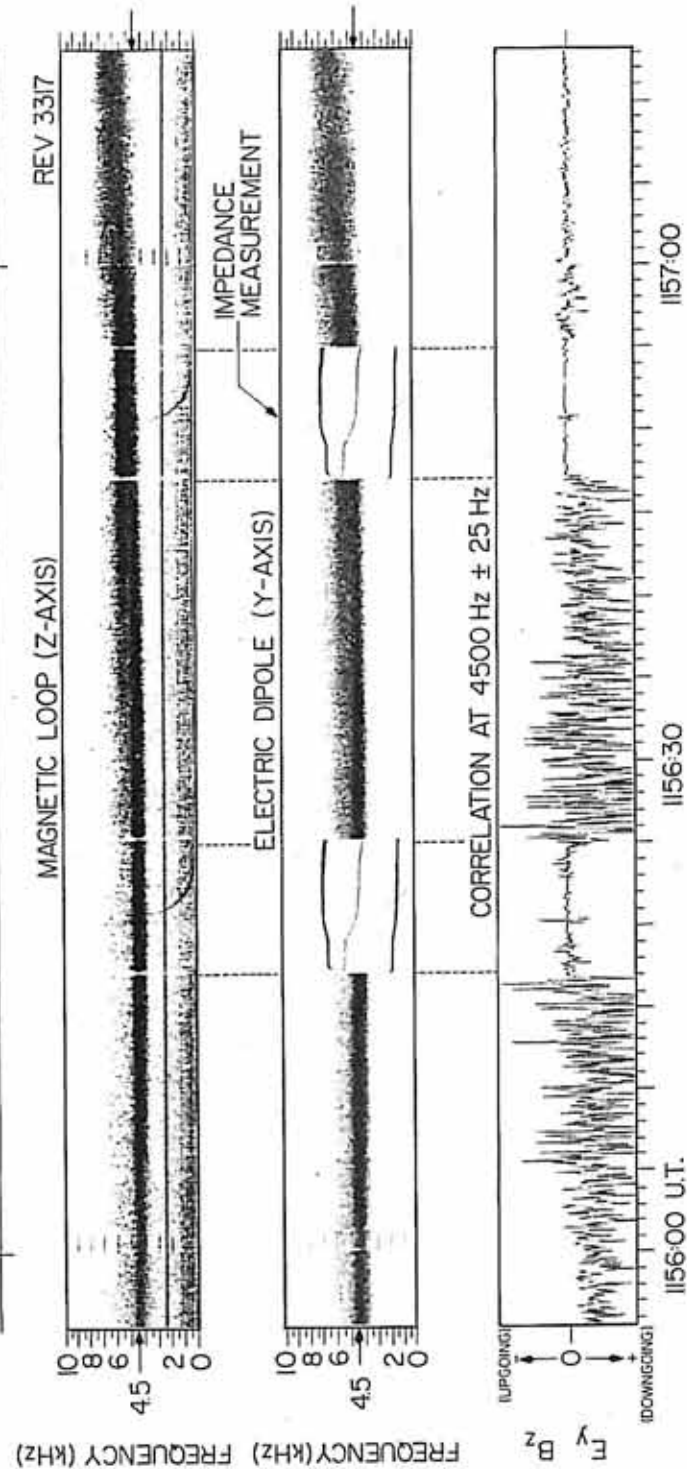
FIGURE 20

Figure 21.   Correlation measurement of mid-latitude VLF hiss,
              showing both downgoing and upgoing waves. This
              type of hiss is observed at latitudes below about
              65° INVL.

C-G69-714-1

REV 3317

602°
2392 KM
3.36 HR

IMPEDANCE
MEASUREMENT

MAGNETIC LOOP (Z-AXIS)

ELECTRIC DIPOLE (Y-AXIS)

CORRELATION AT 4500 Hz ± 25 Hz

62.0° INVARIANT LATITUDE
2368 KM ALTITUDE
3.22 HR MAGNETIC LOCAL TIME

FREQUENCY (kHz)   FREQUENCY (kHz)

E_y B_z

1156:00 U.T.   1156:30   1157:00

MAY 8, 1969

FIGURE 21

Figure 22.   Correlation measurement of saucer-shaped emission,
             showing only upgoing waves. The outer envelope is
             sharply defined and nearly symmetric about the
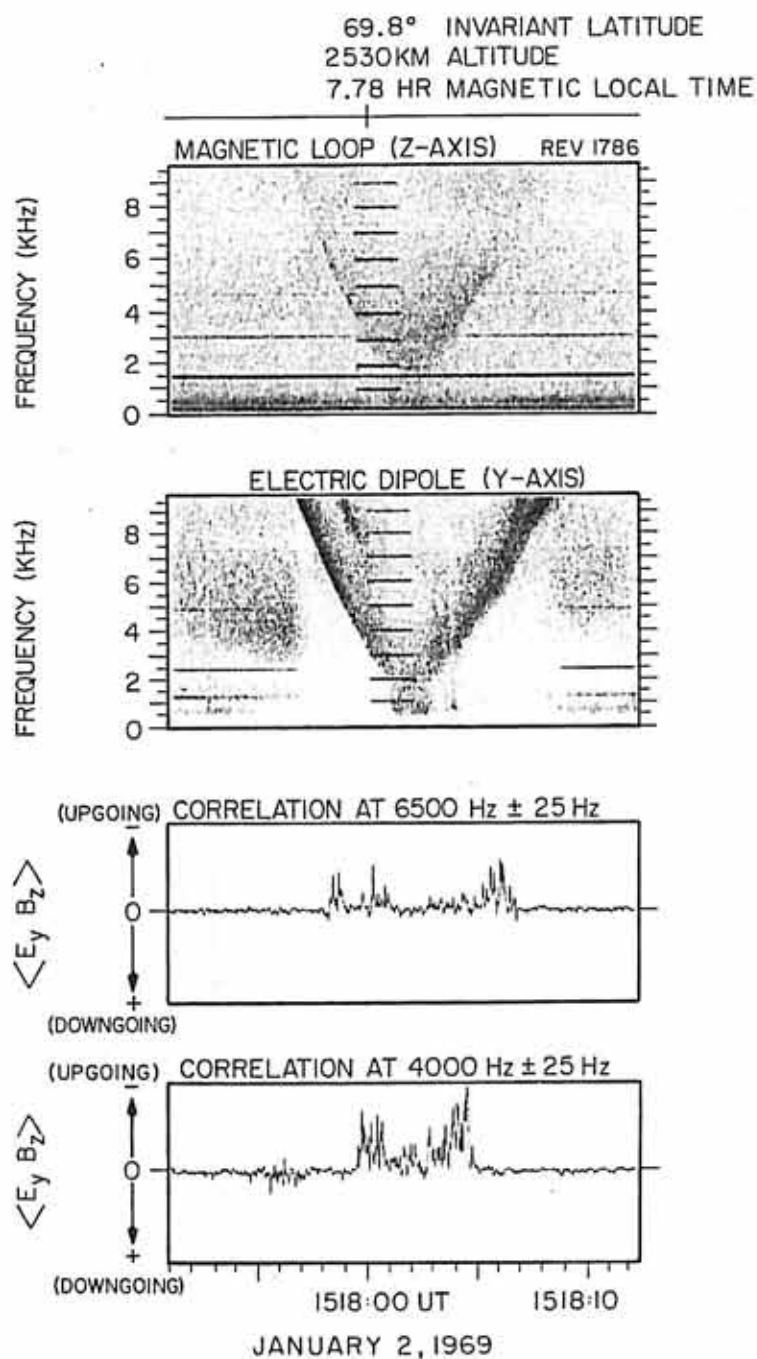   minimum frequency of emission.

A-G69-404-3

69.8° INVARIANT LATITUDE
2530 KM ALTITUDE
7.78 HR MAGNETIC LOCAL TIME

FIGURE 22

Figure 23.   Correlation measurement of asymmetric saucer-shaped

emission.   Only upgoing waves are observed.

73.4° INVARIANT LATITUDE
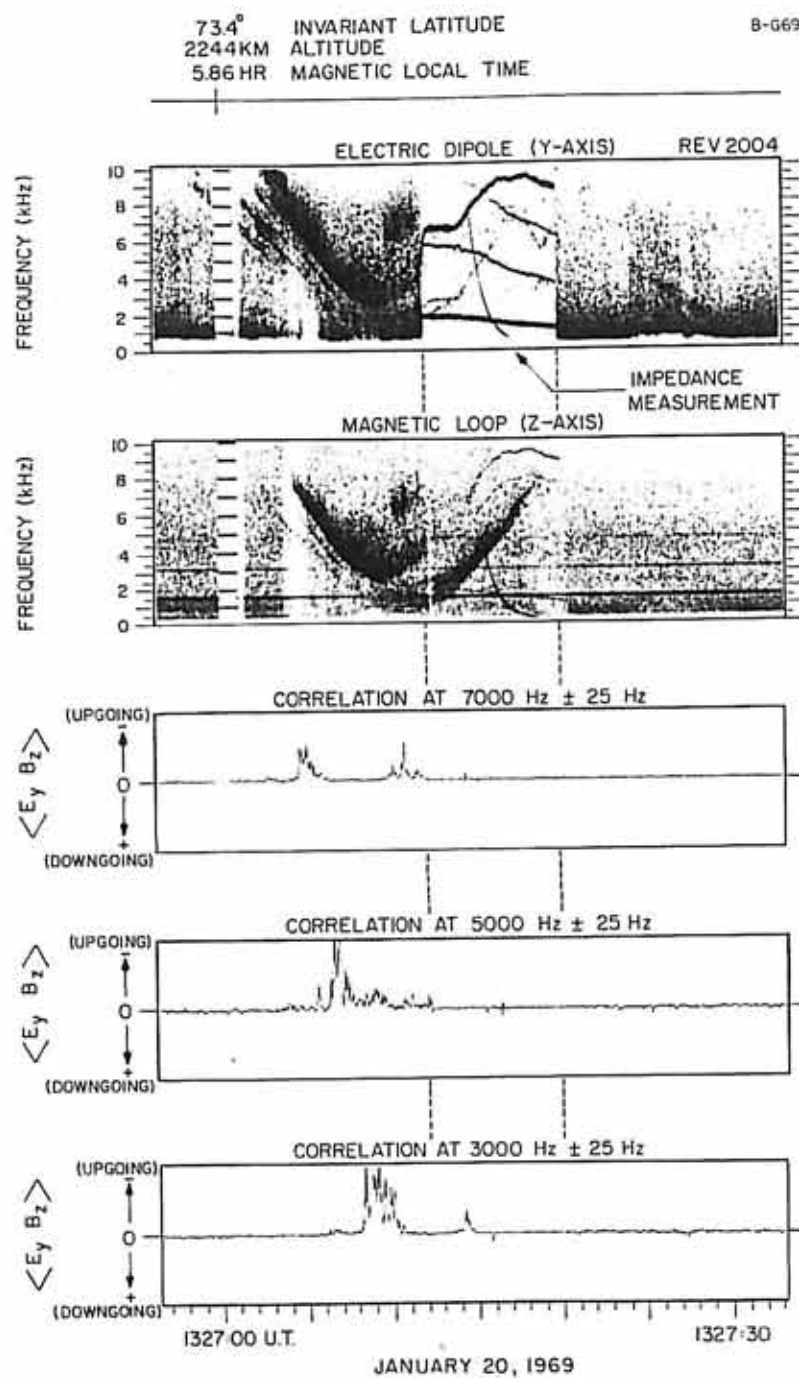2244KM ALTITUDE
5.86 HR MAGNETIC LOCAL TIME

B-G69-712-1

ELECTRIC DIPOLE (Y-AXIS)　　REV 2004

IMPEDANCE
MEASUREMENT

MAGNETIC LOOP (Z-AXIS)

CORRELATION AT 7000 Hz ± 25 Hz

CORRELATION AT 5000 Hz ± 25 Hz

CORRELATION AT 3000 Hz ± 25 Hz

1327:00 U.T.　　　　　　1327:30

JANUARY 20, 1969

FIGURE 23

Figure 24.   Correlation measurement of narrow, multiple saucer-
shaped emissions.   The narrow envelopes suggest that
the source was near the satellite altitude.

A-G69-745-1

INVARIANT LATITUDE   74.5°
ALTITUDE   1986 KM
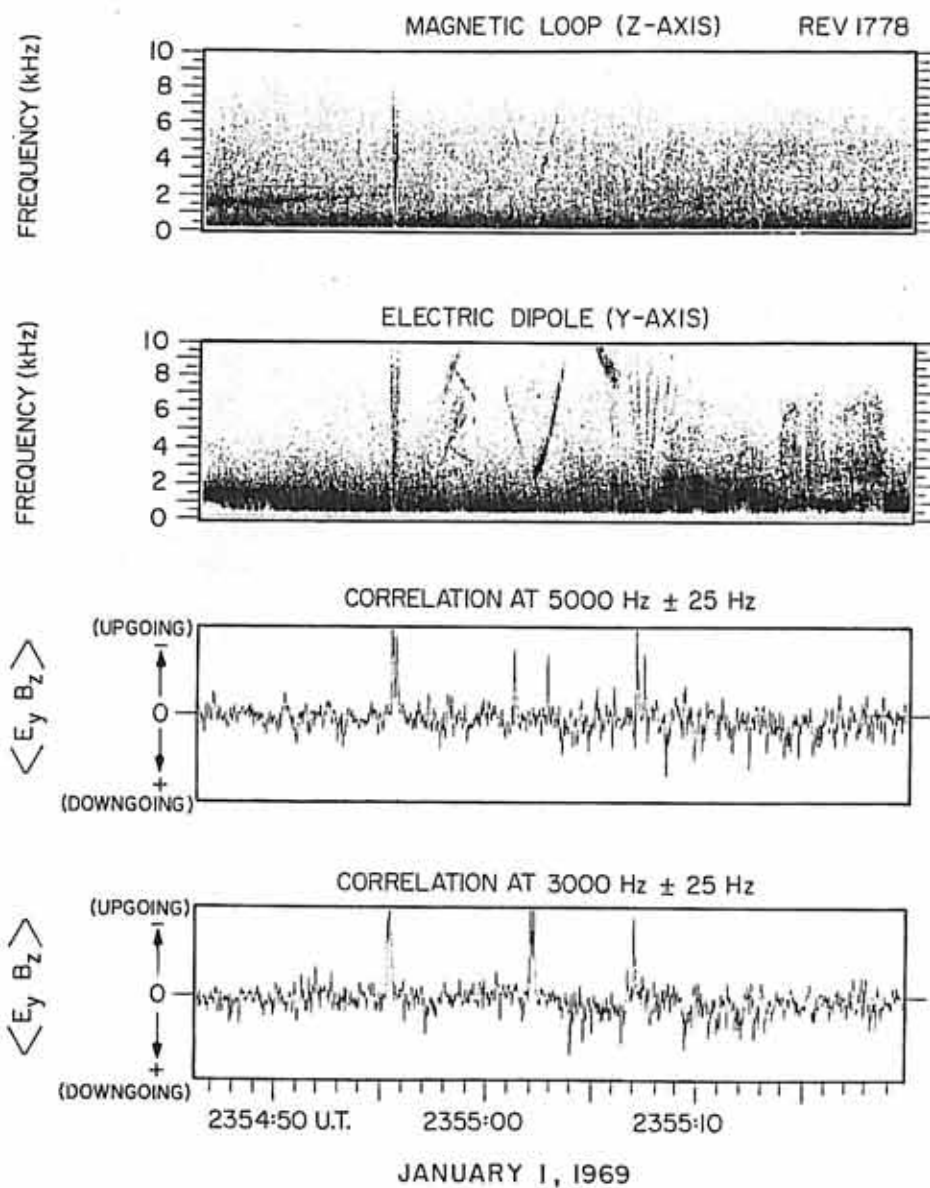MAGNETIC LOCAL TIME   17.78 HR

MAGNETIC LOOP (Z-AXIS)   REV 1778

ELECTRIC DIPOLE (Y-AXIS)

CORRELATION AT 5000 Hz ± 25 Hz

CORRELATION AT 3000 Hz ± 25 Hz

2354:50 U.T.   2355:00   2355:10

JANUARY 1, 1969

FIGURE 24

Figure 25. Refractive index surfaces and ray paths for the

saucer-shaped emission in a homogeneous ionosphere,
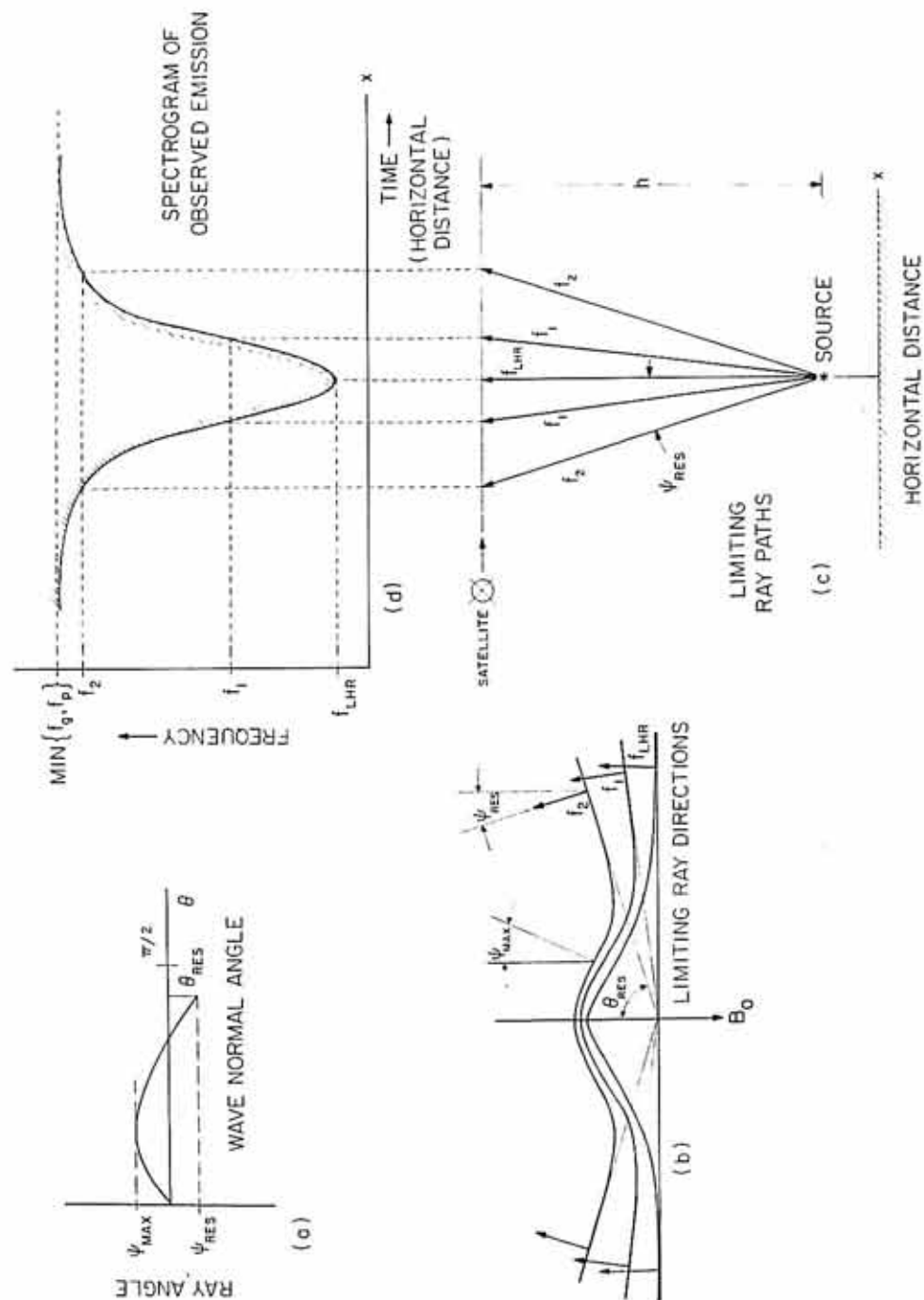
showing the resulting frequency-time spectrogram.

FIGURE 25

Figure 26.   Ray paths for the saucer-shaped emission for an

ionosphere in which the plasma frequency and IHR

frequency decrease monotonically with increasing

altitude, showing the resulting "gap" in the
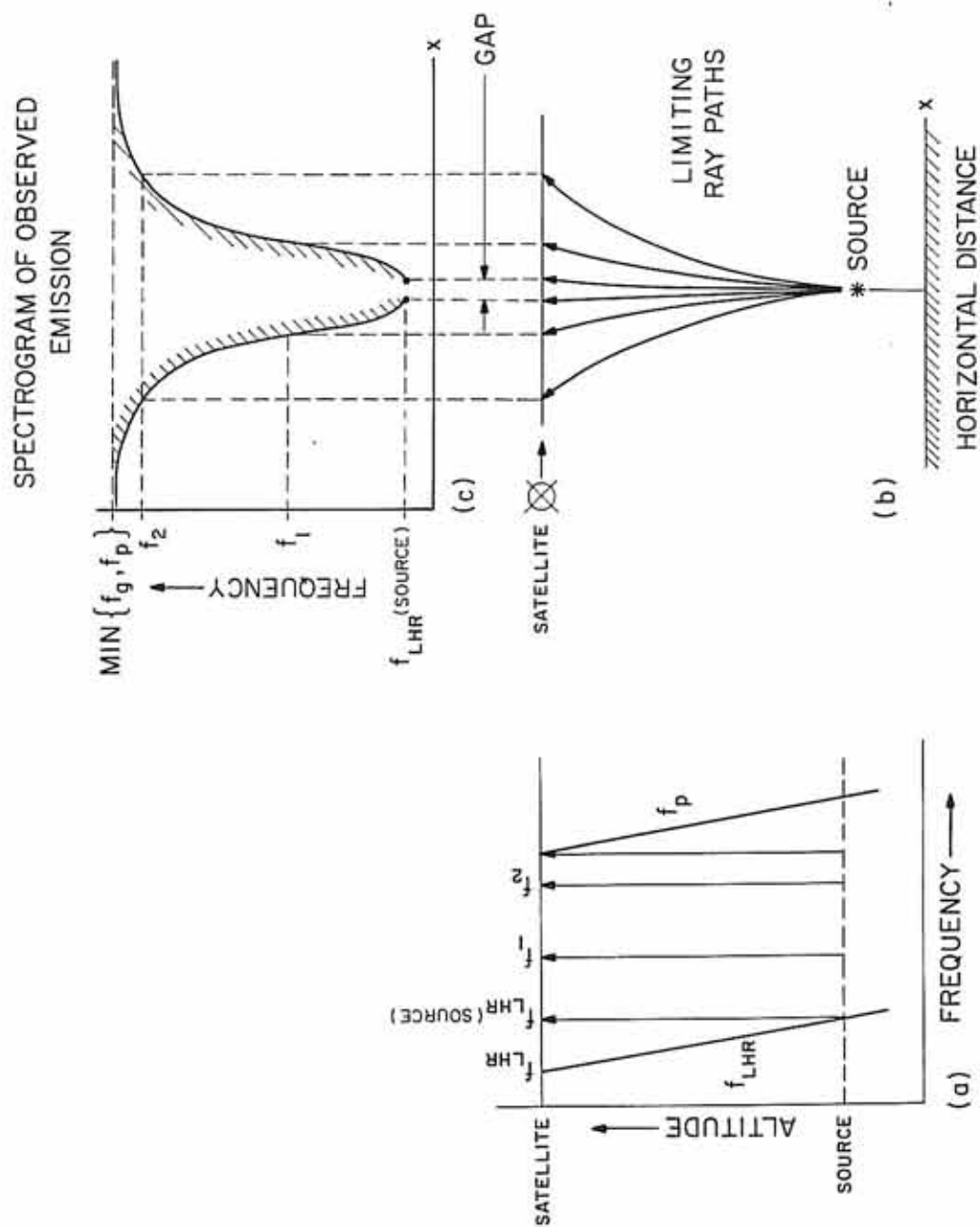
frequency-time spectrogram.

116

C-G69-464

SPECTROGRAM OF OBSERVED EMISSION

GAP

LIMITING RAY PATHS

(c)

(b)

FIGURE 26

Figure 27. Block diagram showing the prelaunch phase calibration procedure for the wideband electric and magnetic receivers aboard Injun 5.
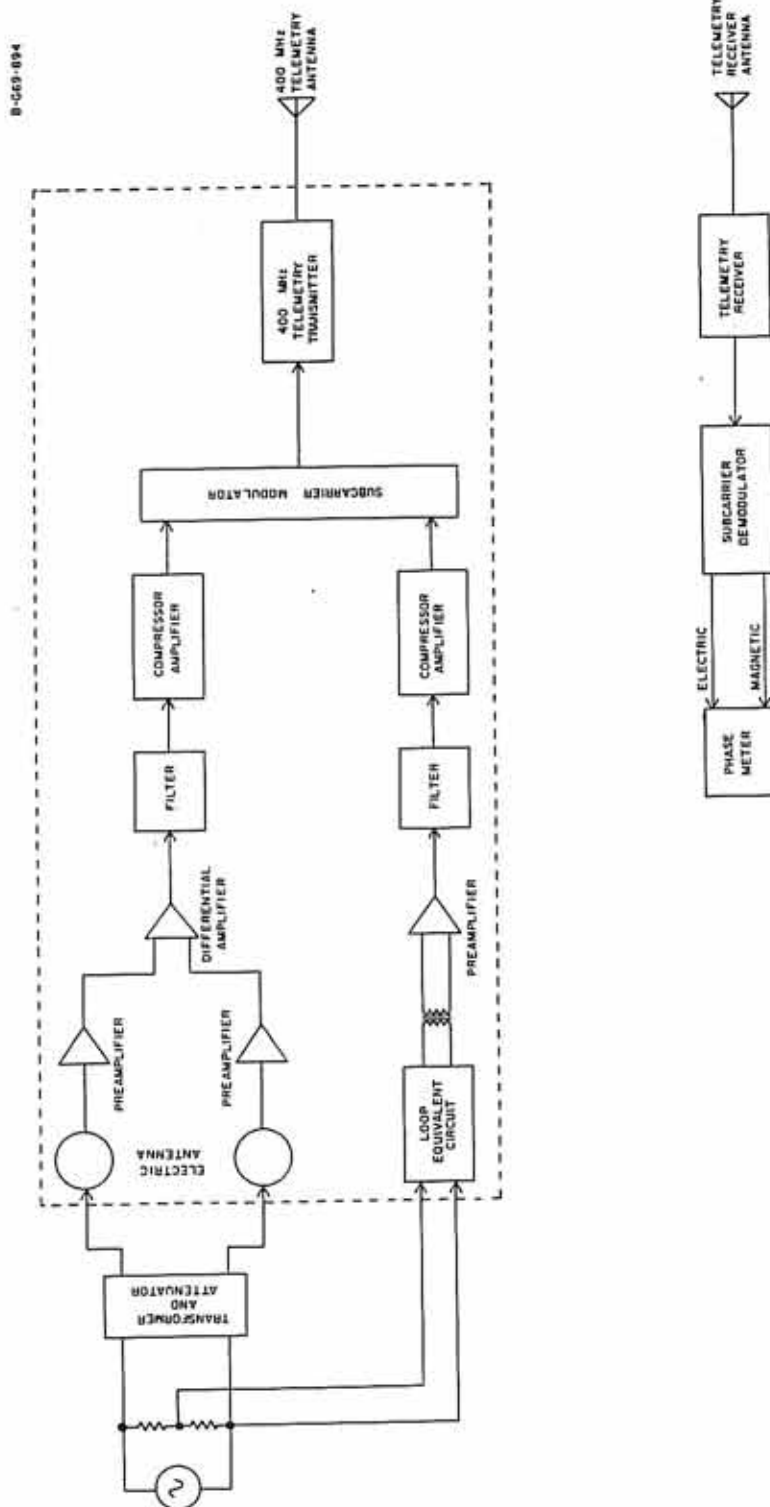
FIGURE 27

Figure 28.   Phase shift calibrations for the low-band receivers, telemetry, and demodulator systems.
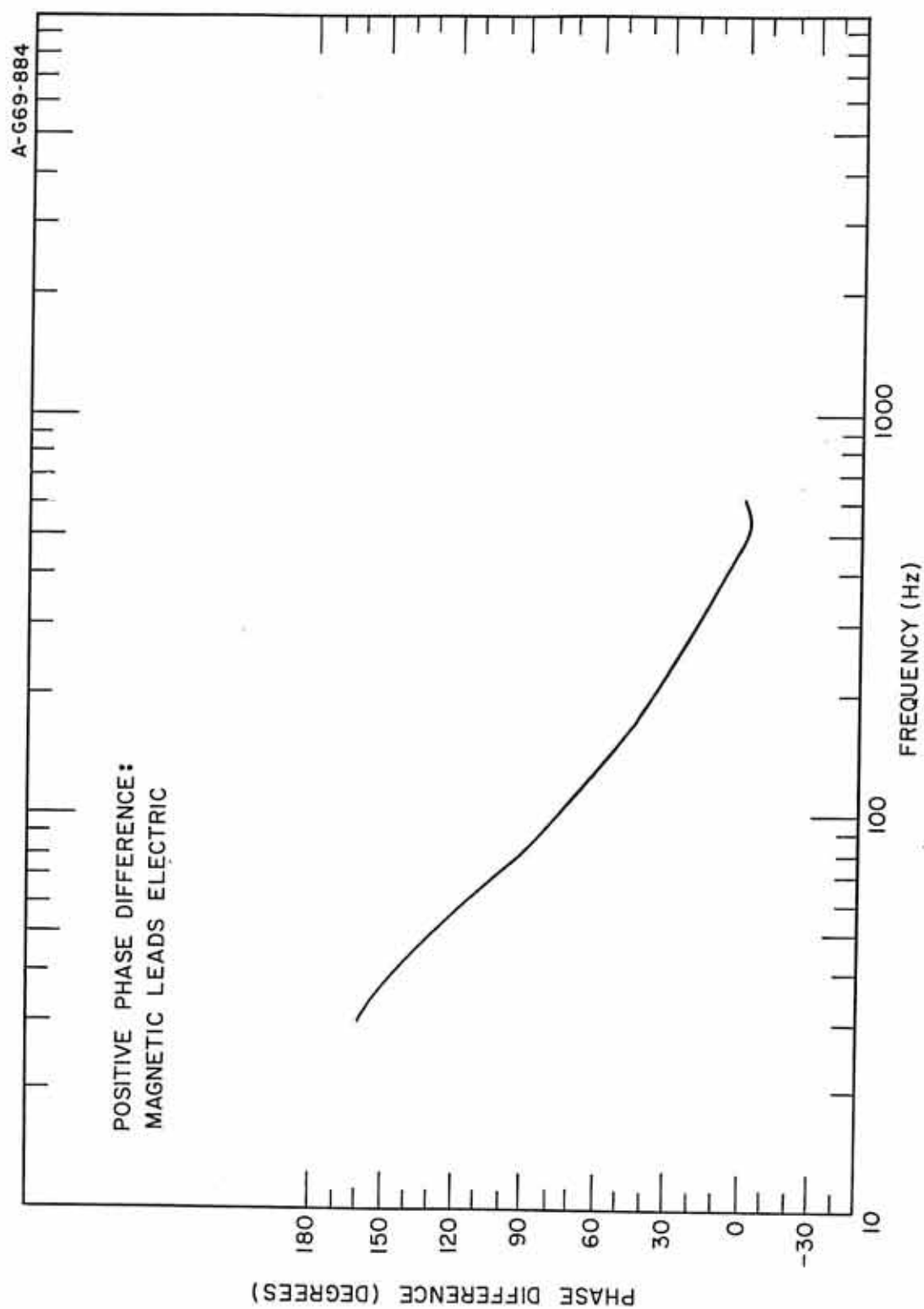
FIGURE 28

Figure 29.   Phase shift calibrations for the high-band receivers,
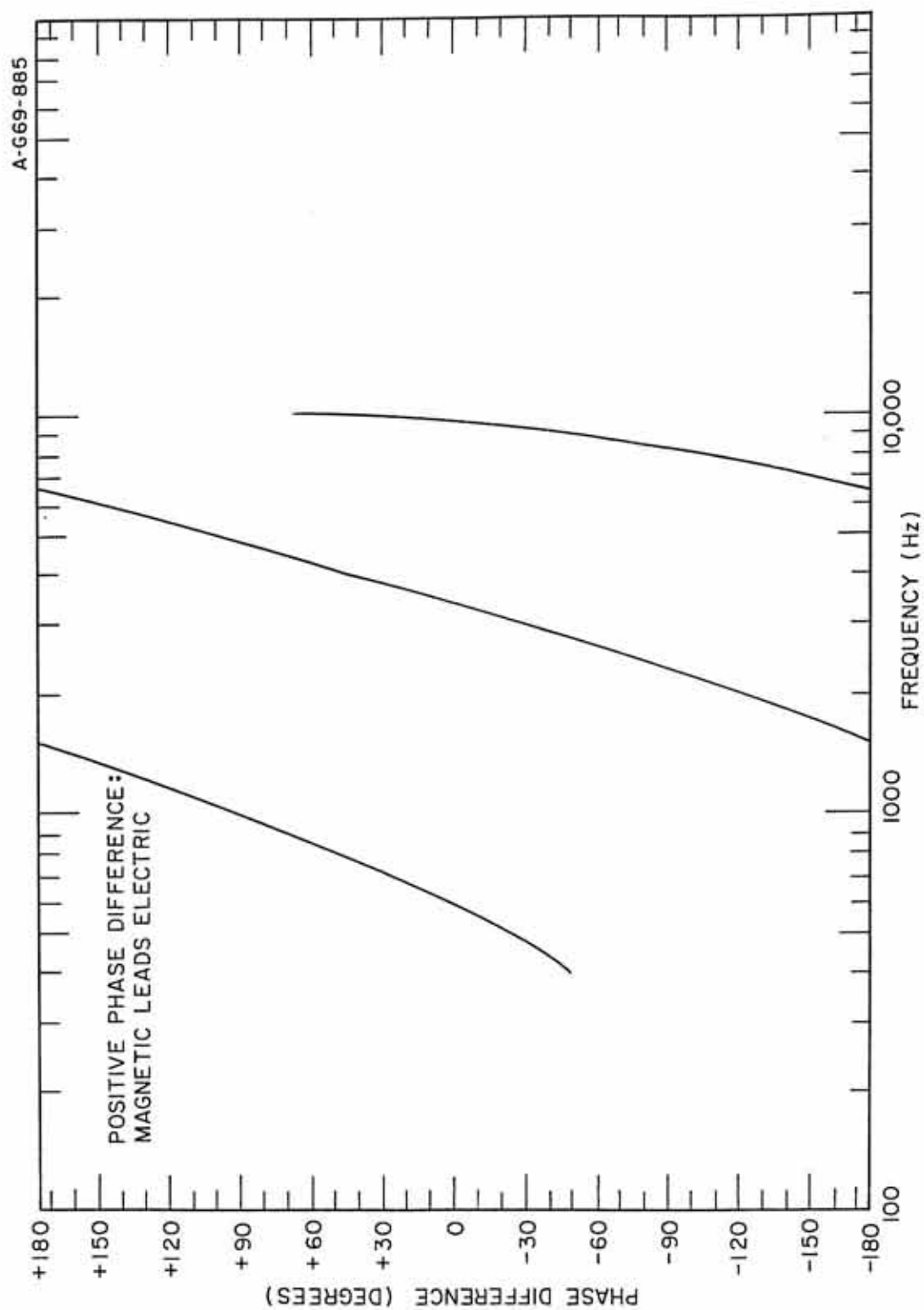telemetry, and demodulator systems.

FIGURE 29